Monthly Notices of the ROYAL ASTRONOMICAL SOCIETY
MNRAS **456,** 2221–2259 (2016) doi:10.1093/mnras/stv2767

H-ATLAS/GAMA: the nature and characteristics of optically red galaxies detected at submillimetre wavelengths

A. Dariush,[1★] S. Dib,[2★] S. Hony,[3★] D. J. B. Smith,[4] S. Zhukovska,[5] L. Dunne,[6,7] S. Eales,[8] E. Andrae,[9] M. Baes,[10] I. Baldry,[11] A. Bauer,[12] J. Bland-Hawthorn,[13] S. Brough,[14] N. Bourne,[7] A. Cava,[15] D. Clements,[16] M. Cluver,[17] A. Cooray,[18] G. De Zotti,[19] S. Driver,[20,21] M. W. Grootes,[9] A. M. Hopkins,[12] R. Hopwood,[16,22] S. Kaviraj,[16,23] L. Kelvin,[24] M. A. Lara-Lopez,[25] J. Liske,[26] J. Loveday,[27] S. Maddox,[6] B. Madore,[28] M. J. Michałowski,[29] C. Pearson,[22,23,30] C. Popescu,[31,32] A. Robotham,[20] K. Rowlands,[21] M. Seibert,[28] F. Shabani,[33] M. W. L. Smith,[8] E. N. Taylor,[34] R. Tuffs,[9] E. Valiante[8] and J. S. Virdee[23,30]

Affiliations are listed at the end of the paper

Accepted 2015 November 23. Received 2015 November 17; in original form 2015 February 24

ABSTRACT

We combine *Herschel*/SPIRE submillimetre (submm) observations with existing multiwavelength data to investigate the characteristics of low-redshift, optically red galaxies detected in submm bands. We select a sample of galaxies in the redshift range $0.01 \le z \le 0.2$, having $>5\sigma$ detections in the SPIRE 250 μm submm waveband. Sources are then divided into two sub-samples of *red* and *blue* galaxies, based on their UV-optical colours. Galaxies in the *red* sample account for ≈4.2 per cent of the total number of sources with stellar masses $M_* \gtrsim 10^{10}$ M$_\odot$. Following visual classification of the *red* galaxies, we find that ≳30 per cent of them are early-type galaxies and ≳40 per cent are spirals. The colour of the *red*-spiral galaxies could be the result of their highly inclined orientation and/or a strong contribution of the old stellar population. It is found that irrespective of their morphological types, *red* and *blue* sources occupy environments with more or less similar densities (i.e. the Σ_5 parameter). From the analysis of the spectral energy distributions of galaxies in our samples based on MAGPHYS, we find that galaxies in the *red* sample (of any morphological type) have dust masses similar to those in the *blue* sample (i.e. normal spiral/star-forming systems). However, in comparison to the *red*-spirals and in particular *blue* systems, *red*-ellipticals have lower mean dust-to-stellar mass ratios. Besides galaxies in the *red*-elliptical sample have much lower mean star formation/specific star formation rates in contrast to their counterparts in the *blue* sample. Our results support a scenario where dust in early-type systems is likely to be of an external origin.

Key words: galaxies: general – submillimetre: galaxies.

1 INTRODUCTION

Galaxies display a wide variety of physical and observational properties. It is well known that the distribution of galaxy optical colours is bimodal, e.g. blue cloud versus the red sequence (Strateva et al. 2001; Baldry et al. 2004; Taylor et al. 2015). The bimodality of the galaxy population exists at least out to $z \simeq 1$ (e.g. Bell et al. 2004b; Tanaka et al. 2005; Cooper et al. 2006; Cucciati et al. 2006; Willmer et al. 2006). A number of different mechanisms (taking place in different environments) have been proposed for the observed bimodality of the galaxy population, including, but not limited to, galaxy merging (major and minor), galaxy strangulation and harassment, ram-pressure stripping as well as AGN feedback (e.g. Mulchaey 2000; Croton et al. 2006; Conselice 2014). Such mechanisms could

★E-mail: ali.a.dariush@gmail.com (AD); sdib@nbi.dk (SD); sacha.hony@free.fr (SH)

regulate the observed optical colours of galaxies by influencing their key physical parameters such as star formation history, mean age of stellar populations, the amount of dust attenuation, dust geometry and metallicity (Bruzual & Charlot 2003; Burgarella, Buat & Iglesias-Pàramo 2005; da Cunha, Charlot & Elbaz 2008; Conroy, Gunn & White 2009).

Besides, there are substantial differences between galaxy populations in the field and those in clusters and groups. According to Dressler (1980), galaxy morphology is a strong function of galaxy density, i.e. the morphology–density relation, and numerous studies since then have shown the dependence of galaxy properties on the local environment (Binggeli, Tammann & Sandage 1987; Lewis et al. 2002; Balogh et al. 2004; Ball, Loveday & Brunner 2008). For example, the red population is substantially dominated by early-type galaxies and thus preferentially found in high-galaxy density environments, while blue galaxies are predominantly late-type systems and mostly found in low-galaxy density environments, i.e. the colour–density relation. Moreover, vast majority of galaxies in the blue cloud are actively forming stars, while the red sequence consists mainly of passive galaxies with little or no ongoing star formation. There are also additional contributions to the red cloud from (a) heavily obscured star-forming or edge-on galaxies and (b) galaxies with passive discs, e.g. red spirals showing signs of low level of star formation, which are known to be considerably redder and more massive than their blue/star-forming counterparts (van den Bergh 1976; Wolf et al. 2009; Masters et al. 2010; Cortese 2012). It is noteworthy that the morphology–density and colour–density relations evolve with redshift (e.g. Butcher & Oemler 1984; Poggianti et al. 2009, 2010).

Analyses of the dust attenuation in active/star-forming galaxies suggest that in contrast to passive galaxies, they are heavily affected by dust (Driver et al. 2007; Johnson et al. 2007; Wyder et al. 2007; Cortese et al. 2008; Tojeiro et al. 2009; Grootes et al. 2013). It has been shown that the bulk of the dust in late-type galaxies is in the cold phase and as consequence emits at >100 μm, i.e. the far-infrared (FIR) and submillimetre (submm) wavelengths (Sodroski et al. 1997; Odenwald et al. 1998; Dunne & Eales 2001; Popescu et al. 2002; Popescu & Tuffs 2002; Vlahakis, Dunne & Eales 2005; Dale et al. 2007, 2012; Bendo et al. 2012). Such wavelengths are covered by the instruments on board the *Herschel Space Observatory* (Pilbratt et al. 2010),[1] Thus, the data collected by *Herschel* is uniquely suited to probe the dusty component, e.g. its characteristics and origin, in all type of galaxies, in particular early-type galaxies which contain significantly less dust than late-type systems.

The existence of dust in early-type galaxies has been first reported from studying the absorption of stellar light (Bertola & Galletta 1978; Ebneter & Balick 1985; Goudfrooij et al. 1994) and since then several studies have been conducted in order to shed light on the quantitative dust content of eary-type galaxies (Knapp et al. 1989; Leeuw et al. 2004; Temi et al. 2004; Temi, Brighenti & Mathews 2007; Savoy, Welch & Fich 2009). However, submm data provided by *Herschel* have enabled us to study dust properties, e.g. its total luminosity, mass and temperature in early-type galaxies in an unprecedented manner due to a better sensitivity, resolution and/or the long wavelength coverage necessary (Boselli et al. 2010; Davies et al. 2010; De Looze et al. 2010; Smith et al. 2012b; Auld et al. 2013; di Serego Alighieri et al. 2013).

[1] *Herschel* is an ESA space observatory with science instruments provided by European-led Principal Investigator consortia and with important participation from NASA.

Among various surveys, the *Herschel* Astrophysical Terahertz Large Area Survey (H-ATLAS; Eales et al. 2010) is the widest extragalactic survey undertaken in submm with *Herschel*. The large coverage of H-ATLAS helps to have a better statistical view of the dust content and its characteristic among galaxies spanning a broad range of luminosities, colours and morphologies. Results from Dariush et al. (2011) as part of the H-ATLAS Science Demonstration Phase (SDP) and based on the UV-optical colour classification, show that the majority of sources ($\simeq$ 95 per cent) with submm detections at low redshift ($z \le 0.2$), are blue/star-forming galaxies with UV-optical colours NUV$-r \le 4.5$. This earlier study suggested that the submm-detected/optically red galaxies (NUV$-r > 4.5$), with a contribution of $\lesssim$5 per cent to the total number of detections, are more likely to be star-forming galaxies and that their red colours are due to obscuration by dust.

From a stacking analysis at submm wavelengths, Bourne et al. (2012) performed a large-scale statistical study of the submm properties of optically selected galaxies (based on the rest-frame colour $g - r$) at $z \lesssim 0.35$, and found that approximately 20 per cent of low-redshift galaxies in H-ATLAS are red.

In the mean time, there have been several H-ATLAS studies trying to shed light on the existence and properties of dust in early-type galaxies. For instance Rowlands et al. (2012) used data from the H-ATLAS SDP to study dust properties and star formation histories in a sample of low-redshift galaxies ($z \lesssim 0.5$) detected at submm wavelengths. Followed by classification of their sample based on optical morphology, Rowlands et al. (2012) found that $\simeq$4.1 per cent of all detections are early-type systems and that $\simeq$3.8 per cent (19 out of 496) of spiral galaxies with submm detections are passive. In another study and by using samples of early-type galaxies at low redshifts ($0.013 \lesssim z \lesssim 0.06$), Agius et al. (2013) found that early-type galaxies with H-ATLAS detections (based on phase 1 version 2.0 internal release of the H-ATLAS catalogue), are not only bluer in the UV-optical colours but also are significantly brighter in NUV in comparison to their H-ATLAS non-detected counterparts.

The aim of this work is to examine in more detail the nature of submm detected red galaxies using the data of H-ATLAS. The main difference between this work and those conducted by Rowlands et al. (2012) and Agius et al. (2013) is that all sources in our sample are detected in H-ATLAS and classified by means of the UV-optical colour index. Our main objectives are: to segregate intrinsically red galaxies from heavily obscured star-forming galaxies, and subsequently discuss the origin and the role of the dust in passive systems. The main improvements compared to our previous study come from:

(i) a larger area coverage (by a factor of ~10) and therefore a better statistics;

(ii) the inclusion of complimentary wavelengths in the mid-infrared (MIR) bands;

(iii) the extraction of various physical parameters from multi-wavelengths observations of sources by means of the spectral energy distribution (SED) fitting.

The paper is organized as following: In Section 2, we present the data from H-ATLAS phase 1 and select a sample of low-redshift galaxies, all detected with *Herschel* in the SPIRE 250 μm submm band. In Section 3, we select sub-samples of optically blue and red galaxies and analyse their physical characteristics such as star formation activities and dust properties as inferred from fitting their SEDs. Our main finding and conclusion are given in Section 4. Throughout the paper, we assume a concordance cold dark matter cosmology with $H_0 = 70$ km s^{-1} Mpc^{-1}, $\Omega_{\rm m} = 0.3$ and $\Omega_\Lambda = 0.7$.

2 DATA

We use data from the H-ATLAS phase 1 version 3.0 internal release which contains the IDs of $>5\sigma$ SPIRE detections at 250 μm and is reduced in a similar way to the SDP data, as described by Ibar et al. (2010), Pascale et al. (2011), Rigby et al. (2011) and Smith et al. (2011). The phase 1 ID catalogues have been produced in a similar way to Smith et al. (2011) and will be presented in Bourne et al. (in preparation).

Initially observed time-line data from SPIRE and PACS instruments were processed by using the Herschel Interactive Processing Environment (HIPE) based on a custom reduction scripts. High-pass filtering was then applied to the data time-lines in order to correct the thermal drift in bolometer arrays. Cross-scan time-line observations were projected by using the naive map-making method of HIPE. For point like sources, catalogue of $>5\sigma$ submm fluxes were produced from the 250 μm PSF filtered map, using the MADX algorithm (Maddox et al. in preparation), as described in Rigby et al. (2011). For extended sources, larger apertures were chosen such that they match the extent of the source submm emission. For each 250 μm source, corresponding 350 and 500 μm flux densities were estimated by using the 350 and 500 μm maps (noise-weighted/beam-convolved) at the source position extracted from the 250 μm map. Finally, 100 and 160 μm aperture flux densities were measured following matching each 250 μm source to the nearest PACS sources within a radius of 10 arcsec. A likelihood-ratio analysis (Sutherland & Saunders 1992) was performed by Bourne et al. (in preparation) to match 250 μm sources to the SDSS DR7 (Abazajian et al. 2009) sources brighter than $r = 22.4$ mag within a 10 arcsec radius. The probability that an optical source is associated with the submm source has been used to define the reliability of an association. According to Bourne et al. (in preparation), objects with reliability $\geq$0.8 are considered to be true matches to submm sources.

The H-ATLAS fields are along the celestial equator centred at RA of 9 h(G09), 12 h(G12) and 14.5 h(G15). 144 deg^2 out of the 161 deg^{2}covered by H-ATLAS overlap with the Galaxy and Mass Assembly (GAMA I) survey (Driver et al. 2009, 2011). The GAMA survey re-processes and combines optical data from the Sloan Digital Sky Survey (SDSS DR6; Adelman-McCarthy et al. 2008), NIR data from the UKIRT Infrared Deep Sky Survey (UKIDSS) Large Area Survey (LAS DR4; Lawrence et al. 2007), and UV from the *Galaxy Evolution Explorer* (*GALEX*; Morrissey et al. 2005). The pre-processing of the GAMA, SDSS and UKIDSS archive data is described in detail in Hill et al. (2011). For all galaxies with $r \leq$ 19.4 mag in G09 and G15 as well as $r \leq 19.8$ mag in G12, redshifts have been measured using the Anglo Australian Telescope and for brighter galaxies, redshift estimates are taken from other existing redshift surveys such as SDSS, the 2dF Galaxy Redshift Survey and the Millennium Galaxy Catalogue (Liske et al. 2003; Driver et al. 2005). Furthermore, the GAMA-*WISE* (the *Wide-field Infrared Survey Explorer*; Wright et al. 2010) catalogue adds coverage in four MIR bands at 3.4, 4.6, 12 and 22 μm (Cluver et al. 2014).

In summary, we have at our disposal UV, optical and MIR data as well as redshift estimates for the submm galaxies within the H-ATLAS/GAMA-overlapping area where all submm selected sources in our sample satisfy the following criteria.

(i) They all have $>5\sigma$ submm detected at SPIRE 250 μm.

(ii) They fall within the redshift range $0.01 \leq z \leq 0.2$. We only select objects with a sufficiently reliable spectroscopic determination (i.e. $n_Q \geq 3$; Driver et al. 2011).

(iii) All submm galaxies have a reliability parameter (`reliability` $\geq$0.8) of being associated with an optical counterpart in the SDSS *r*-band catalogue, for which multiwavelength photometry is available. As such, in addition to the 250 μm emission, all sources (7131 objects) have corresponding fluxes (all corrected for Galactic extinction) via aperture matched photometry in other bands ranging from UV to MIR.

(iv) Since a crucial aspect of our selection of red galaxies is based on the UV-optical (NUV$-r$) colour, we remove from our sample those galaxies for which their NUV fluxes as estimated in GAMA, differ by more than >0.5 mag from those retrieved through *GALEX* GR6 Data Release based on the All-Sky Imaging survey (AIS) data products (NUV depth $\sim$20.8 mag). In addition, all selected sources have NUV magnitude errors, as provided by *GALEX*-GR6, which are $\leq$0.2 mag. This guarantees that all sources in our sample have enough signal-to-noise ratio in UV. The above constraints on UV fluxes, reduces our sample to 4016 sources.

(v) Finally, since the physical parameters inferred for each galaxy are based on SED-fitting techniques, an extra criterion has been applied in order to exclude sources (234 in total) with poor-quality SED fits (see Section 3.3).

After applying these selection criteria, we find 3782 galaxies with detections in at least NUV + *u, g, r, i, z* and 250 μm bands. Distributions of the SDSS *r* band and NUV magnitudes for all galaxies as well as those qualified to be included for the subsequent data analysis are shown in panels of Fig. 1. According to the first panel, approximately $\approx$13 per cent of the initial submm sources were excluded following the requirement of a UV detection for inclusion in the sample. But that does not seems to exclude systematically any particular type of sources as a Kolmogorov–Smirnov test (KS test) suggests a $\gtrsim$70.0 per cent probability that the distribution of sources detected at 250 μm is similar to the one being observed simultaneously in the 250 μm+ NUV bands. However by limiting errors in the NUV band to $\lesssim$0.2 mag, more sources ($\approx$31 per cent) are excluded in particular faint objects in the NUV band.

A subset of sources have also detections in *GALEX* FUV, PACS (100, 160 μm) and SPIRE (350, 500 μm) submm bands. *WISE* data are available and recently have been cross-matched, with extended sources from *WISE* accounted for correctly, for all GAMA fields. Yet at the time of analysing galaxy SEDs in this work, *WISE* data were only available for the G12 and G15 fields. Thus, out of the 3782 sources, 2622 ($\approx$70 per cent) have also aperture-matched *WISE*-MIR data.

3 ANALYSIS

3.1 Selection of intrinsically red objects

Though the vast majority of galaxies at low redshift with submm detection are star forming and optically blue, a small fraction of them are red in optical bands (e.g. $u-r$, $g-r$). We separate blue and red galaxies in the sample using the UV-optical index. This is more robust than optical colour indices as it is more sensitive to recent star formation activity (e.g. Kaviraj et al. 2007). Dariush et al. (2011) separate red and blue galaxies in the H-ATLAS sample at NUV$-r = 4.5$, estimated through fitting a double Gaussian to the NUV$-r$ colour distribution of galaxies, with redshifts $0.01 \leq z \leq 0.2$ (i.e. similar to this work), in the H-ATLAS SDP data. Hence any source with NUV$-r \geq 4.5$ mag is considered as *red*, while *blue* objects are those with NUV$-r < 4.5$ mag. As Fig. 1(a) shows, the

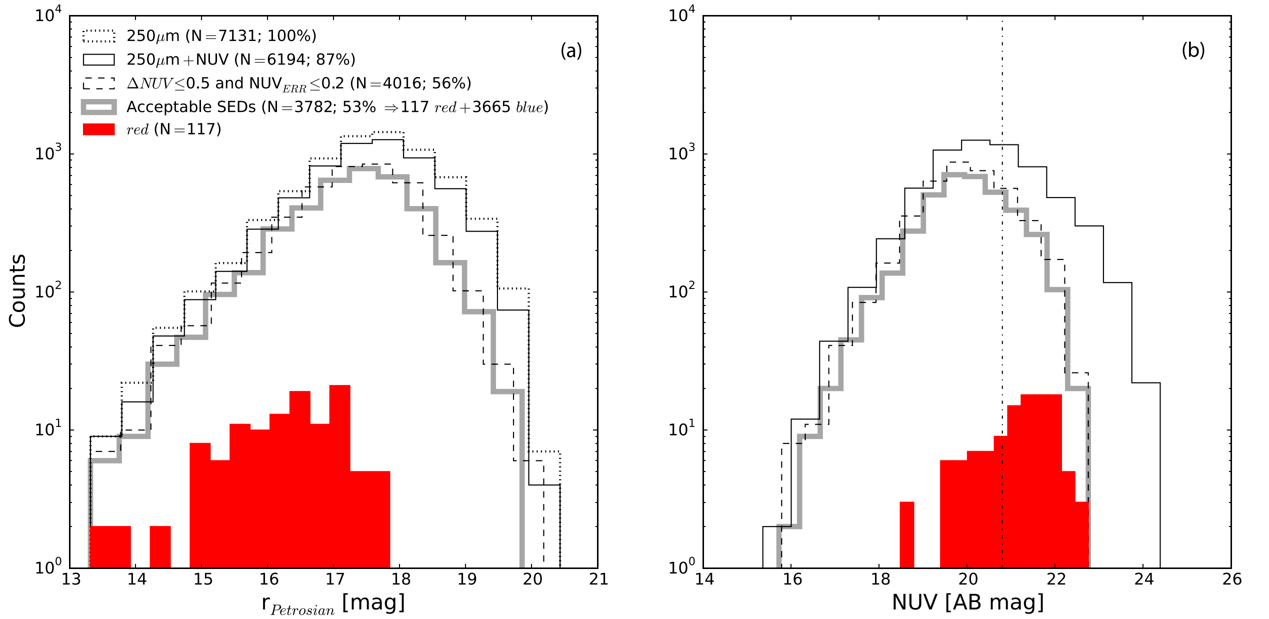

Figure 1. Distributions of the SDSS *r* band (panel a) and NUV (panel b) magnitudes for all galaxies as well as those qualified to be included for the subsequent data analysis. 'Dotted line' represents all galaxies detected in 250 μm while the 'black solid line' shows those observed in NUV with a subset of them (dashed line) having NUV errors ≤0.2 and ΔNUV≤0.5 (i.e. the absolute difference between the GAMA and *GALEX* NUV flux measurements). Finally, the 'grey thick line' represents sources with good quality SED fits as described in Section 3.3. Sources were also divided into two categories of red (filled histogram) or blue based on their UV-optical NUV−*r* colours as discussed in Section 3.1. The vertical 'dash–dotted' line in panel (b) shows the *GALEX* AIS (All-Sky Imaging Survey) NUV depth which is around ≈20.8 mag.

majority of the *red* galaxies in our sample have apparent *r*-band magnitudes $\lesssim$17.5 mag and NUV magnitudes $\gtrsim$19.0 mag.

3.1.1 Contamination by radio AGN

In order to ensure that none of the submm emission has been contaminated by synchrotron emission from radio jets hosted by active galactic nuclei (AGNs), we find and exclude radio AGN as follows. We cross-matched the SDSS position of our sources with those from the full, unfiltered radio-source catalogue of Virdee et al. (2012). The radio catalogue consists of all sources detected in the H-ATLAS phase 1 field by the NRAO VLA Sky Survey (Condon et al. 1998) and, as such, contains 7823 sources. The outcome is 117 matches having separations of <1.0 arcsec. In order to determine whether the radio emission was consistent with the presence of a radio-loud AGN, we calculated q_{250}, defined as

$$q_{250} = \log_{10}\left(\frac{S_{250}}{S_{1.4}}\right), \quad (1)$$

where S_{250} and $S_{1.4}$ are fluxes at 250 μm and 1.4 GHz for all matched sources, respectively. If $q_{250} < 1.4$ then part of the radio emission is due to AGN activity (Jarvis et al. 2010). Conservatively, we exclude any source which satisfies this criterion in order to ensure none of the submm emission may be contaminated by radio AGN activity. Out of 117 sources with radio counterparts, only 13 sources (1 *red* and 12 *blue* galaxies) have $q_{250} < 1.4$ and are thus excluded from the subsequent analysis.

3.1.2 Morphology of the red galaxies

The SDSS postage-stamp images of all *red* sources together with their SEDs (inferred as described in Section 3.3) are presented in Appendix A.

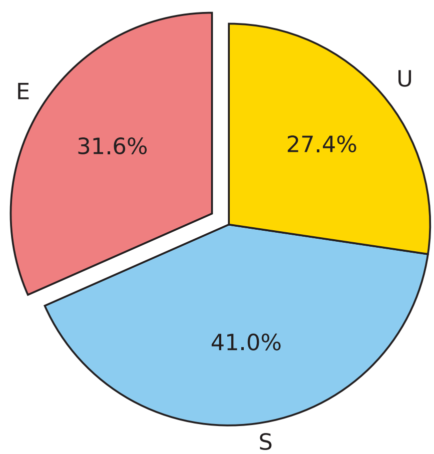

Figure 2. Percentage of each morphological type in the sample of 117 red galaxies (see Section 3.1.2). Labels represent elliptical (E), spiral (S) and undefined (U) galaxies.

The morphology of all 117 galaxies were examined from their SDSS *r*-band images, following independent visual inspection by three team members. Galaxies were classified into three categories of elliptical (E), spiral (S) and uncertain (U). The number of sources in each morphological type is 37, 48 and 32 for the E, S and U galaxies, respectively (see Fig. 2). Many of the sources classified as U are too small in the SDSS images to judge their morphology and can be of any type, i.e. spiral, elliptical or merging galaxies.

In order to test the validity of this morphological classification, we compared our classification to an independent morphological classification based on the Sérsic index *n* which we obtained from the SDSS DR7 galaxy catalogue Simard et al. (2011). Different studies have adopted different thresholds of the Sérsic index above/below

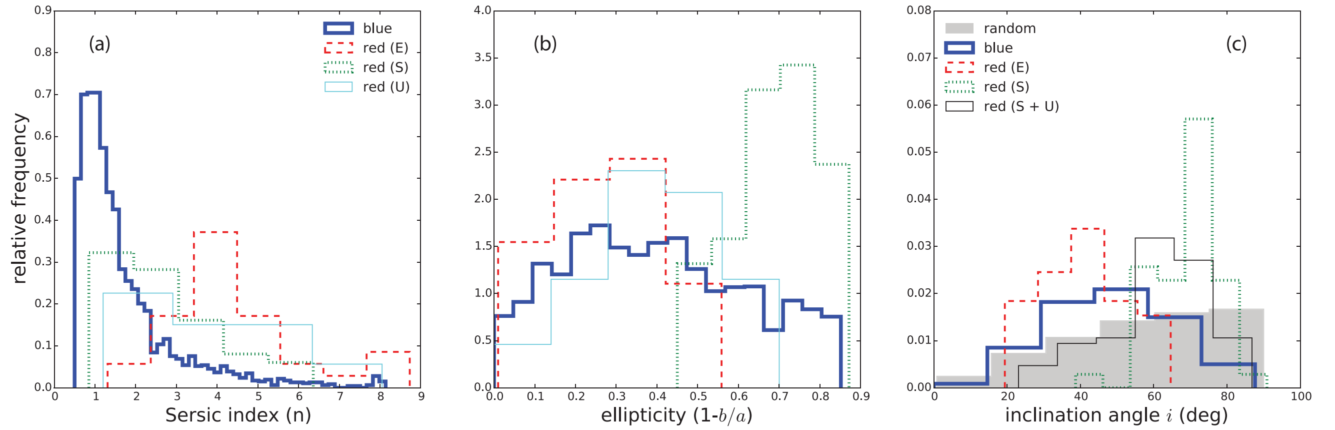

Figure 3. Distributions of morphology related parameters in all blue (thick solid line) and red sources. E (red dashed line), S (green dotted line) and U (cyan line) labels represent the morphology of individual red source as explained in Section 3.1.2. Each histogram is normalized by its integral. Panels represent distributions of galaxy (a) Sérsic index, (b) ellipticity and (c) inclination angle. In addition, the 'black dotted line' and 'grey filled histogram' in panel (c) represent the distribution of *red*-S+R galaxies and random distribution of inclination angles, respectively.

which a galaxy is considered as early/late type. For instance, Ravindranath et al. (2004) adopts $n = 2.0$ to divide their sample into early and late types though Sérsic indices of $n > 2.5$ have been also used to describe early-type sources (e.g. Bell et al. 2004a; Barden et al. 2005).

Fig. 3 (panel a) displays the distributions of Sérsic indices for all galaxies in our sample, i.e. the *blue* sample as well as the morphologically classified *red* galaxies.[2] From this figure, it is clear that the distribution of Sérsic indices for the *red*-E sample peaks around ≈4. This is larger than those estimated for the S galaxies (either *blue* or *red*). The Sérsic index distribution of the *red*-U galaxies lies somewhat between those of the S and E samples.

An inspection of the ellipticity parameter[3] of all galaxies in the sample (Fig. 3, panel b) reveals that, not surprisingly, in *red* sources of type S, $e \gtrsim 0.5$ whereas in *red* galaxies of type E, $e \lesssim 0.5$. In fact the disc structure is extremely pronounced in highly inclined spiral galaxies and therefore the majority of galaxies in the S category are those having larger ellipticities. This is better shown in Fig. 3(c) where histograms of galaxy inclination angles (i) for *blue* , *red*-S, *red*-E as well as *red* S+U samples are plotted. Inclinations are determined from the relation

$$\cos^2 i = [(b/a)^2 - p^2](1 - p^2)^{-1} \quad (2)$$

in which p is the ratio of the smallest to the largest axis of an oblate spheroid of rotation. We assume $p = 0.20$ which is an appropriate value to use for the intrinsic flattening of the distribution of the light of galactic spheroids (e.g. van den Bergh 1988).

Unlike *blue* and *red*-E galaxies, the majority of *red*-S galaxies are highly inclined. Note that, even in the combined *red*-U + *red*-S sample, there is still and excess of galaxies with relatively large inclination angles in comparison to the *blue* and *red*-E samples.

To illustrate this, we show in Fig. 3(c) the distribution of inclination angles as expected from a random sampling. The observed difference between the distribution of *red*-(S+U) galaxies in comparison to a sample of simulated inclinations, suggests that the fraction of highly inclined systems in *red*-(S+U) sample is more than one would expect for a random distribution. This shows that the inclination angle play a non-negligible role in the observed red colour of *red*-S systems.

The main conclusion is that the *red*-E sample consists of intrinsically red objects, while the *red*-S sample contains galaxies where inclination could be a dominant factor in determining the observed red optical colours. Although these inclined sources are not the main interest of this paper, we do discuss some of their ensemble properties in Section 3.5.1.

3.2 Environmental density of *red* galaxies

In order to explore the environmental density of *red* galaxies and see if it plays an important role in shaping their observed properties, we compute the projected surface density around each galaxy. This is based on counting the number of nearest neighbours, i.e. the density within the distance to the Nth nearest neighbour. Hence, the surface density to the fifth nearest neighbour is calculated as

$$\Sigma_5(\mathrm{Mpc}^{-2}) = \frac{5}{\pi d_5^2}, \quad (3)$$

where d_5 is the projected comoving distance to the fifth nearest neighbour within a volume-limited density-defining population (DDP) and relative velocity $\pm 1000\ \mathrm{km\,s^{-1}}$ (Wijesinghe et al. 2012; Brough et al. 2013). The DDP are galaxies brighter than $M_r \leq -20.0$. Densities are calculated for galaxies with $r_{\mathrm{Petro}} \leq 19.4$ (where r_{Petro} is the r-band Petrosian magnitude), $0.01 \leq z \leq 0.18$ and with reliable redshifts ($n_Q \geq 3$; Driver et al. 2011). Although equation (3) is a 2D estimate, the redshift information of each galaxy is used to remove the background and foreground sources.

Fig. 4 displays histograms of the projected densities for *blue* and *red* galaxies within the redshift range of $0.01 \leq z \leq 0.18$ and for all systems having $M_r \leq -20.0$. This decreases the overall number of *red* galaxies by ≈4.2 per cent (out of 117 *red* galaxies, two have $z > 0.18$ and three have $M_r > -20.0$). Although the highest observed density ($1.5 \lesssim \log(\Sigma_5) \lesssim 2.5$) is populated by a small fraction of the *red*-E-type systems which indeed are relatively massive galaxies, there is no significant difference between the distribution for the *red* sources in any morphological type with respect to the one corresponding to the *blue* sample. This indicates that all galaxies,

[2] We perform a KS test, associated with different estimated parameters, for each pair of galaxy types. The results (p values) are reported in the KS test Table 1.

[3] The ellipticity for each galaxy has been estimated as ($e = 1 - b/a$) where a and b are the galaxy's semimajor and semiminor axes as measured in the SDSS.

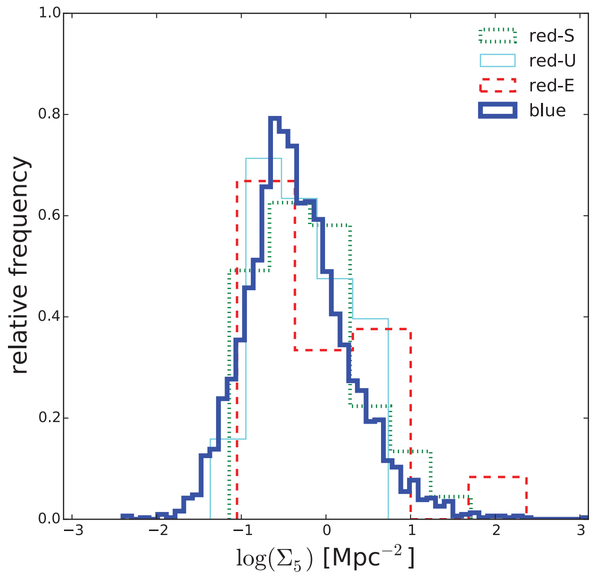

Figure 4. Distributions of the projected surface density Σ_5 estimated according to equation (3) in blue (thick solid line) and red sources. E (red dashed line), S (green dotted line) and U (cyan line) labels represent the morphology of individual red source. Each histogram is normalized by its integral.

irrespective of their morphologies, reside in environments with similar densities. It is worth mentioning however that within the redshift range considered here, the survey area does not contain very dense, cluster-like, environments.

3.3 UV-to-submm SED fitting

We derive the basic properties of galaxies by fitting their SEDs which makes use of the data (Section 2) going from the NUV up to all available *Herschel* bands. The SED of each galaxy is fitted using MAGPHYS (Multi-wavelength Analysis of Galaxy Physical Properties; da Cunha et al. 2008). MAGPHYS infers the galactic properties by matching the observed SED with a large library of calculated SEDs. These templates are constructed by considering the spectral evolution of stellar populations that are born with a Chabrier (2003) initial mass function (IMF) in combination with infrared dust spectral libraries as described in da Cunha et al. (2008). The model assumes that the energy from UV-optical radiation emitted by the stellar populations is absorbed by dust and re-radiated in the FIR. It uses also the two-component dust model of Charlot & Fall (2000) in order to account for the attenuation of starlight by dust. The model also accounts for the enhanced attenuation of stellar radiation for stars located in star-forming regions in comparison to older stars found elsewhere within the galaxy.

As the MAGPHYS analysis is based on AB magnitudes, all available photometry (aperture matched) has been converted to the AB magnitude system before estimating their associated fluxes in units of Jansky (Jy). Additional errors have been added to non-submm fluxes before running MAGPHYS to account for the total flux measurements and calibrations between the different surveys. These include adding 10 per cent of the flux values in quadrature for all optical-NIR bands and 20 per cent for the UV bands. For each output parameter, MAGPHYS produces a probability density function (PDF), in addition to the median value of each PDF. The 16th and 84th percentiles of the PDF have been considered as a measure of the uncertainty.

Smith et al. (2012a) showed that it is insufficient to identify bad SED fits based on a simple χ^2 threshold, instead deriving a threshold which depends on the number of bands of photometry available, above which there is <1 per cent chance that the photometry is consistent with the MAGPHYS model. Sources exceeding this varying threshold are identified as bad fits, and excluded from the subsequent analysis. We use the H-ATLAS SED fits over the entire phase 1 area, derived using the same method as in Smith et al. (2012a), with updated PACS coverage and including data from *WISE*.

For the purpose of our study, we have focused on a number of galactic parameters that are inferred by fitting the observed SEDs with MAGPHYS. These are: the galactic stellar mass (M_*), the dust mass ($M_{\rm D}$), the star formation rate (SFR), and the fraction of total dust luminosity contributed by the diffuse interstellar medium (ISM, f_μ; $0 \leq f_\mu \leq 1.0$). Large values of f_μ indicate that dust is heated by the old stellar populations, while lower values suggest that ongoing star formation has a more prominent role in heating the dust. An example of an SED fit for a submm source in our *red* sample is shown in Fig. 5. We find that the distribution of χ^2 in our sources, does not show any correlation with galaxy NUV$-r$ colour indices. It is worth mentioning that the comparison of the results from MAGPHYS, with and without the MIR constraints from *WISE*, shows that including the *WISE* data modifies the output results from MAGPHYS. The inclusion of *WISE* data improves the fits of the SEDs and provides better estimates of some of the parameter, and notably of the SFR. For this reason, we include in the following sections only those galaxies for which *WISE* data are available (e.g. ≈2/3 of the main sample). This in turn, reduces the size of our sample from 3782 to 2622 sources with 78 having NUV$-r \geq 4.5$ mag and therefore are *red*.

Fig. 6 displays the mass distribution of galaxies in the *blue* and *red* samples (in different categories). In our sample, ≈73 per cent of *blue* sources have stellar masses $\log(M_*/{\rm M}_\odot) \geq 10.0$, while the same number for the *red* galaxies is ≈97 per cent, accounting for ≈4.2 per cent of the total number of sources with $\log(M_*/{\rm M}_\odot) \geq 10.0$. As expected, bins associated with largest stellar masses are occupied by the *red*-E galaxies (see Table 2).

3.4 Dust properties

It is important to compare the inferred parameters derived from MAGPHYS to other determinations. We compare the estimated dust-to-stellar mass ratio ($M_{\rm D}/M_*$) for all sources as computed by MAGPHYS to those derived for a sample of ∼300 nearby galaxies from the HRS (*Herschel* Reference Survey; Cortese et al. 2012). The total dust mass of a given galaxy as estimated by MAGPHYS is the sum of the three components which includes the mass contributed by dust in thermal equilibrium in stellar birth clouds, as well as warm and cold dust components in the ambient ISM (da Cunha et al. 2008).

Fig. 7 displays the distribution of $M_{\rm D}/M_*$ inferred from MAGPHYS for our sample against NUV$-r$ for all *red* and *blue* sources. Overlaid are the $M_{\rm D}/M_*$ estimates from the HRS using all SPIRE bands. For HRS non-detections (triangles), the submm upper-limit fluxes have been determined assuming a 3σ signal over a circular aperture of radius 0.3×, 0.8× and 1.4× of the optical radius for the HRS E, S0 and spirals, respectively.

Note that in determining dust masses $M_{\rm D}$, both MAGPHYS and Cortese et al. (2012) adopt a dust emissivity index $\beta = 2.0$ for cold dust but different dust mass absorption coefficients κ_ν. Cortese et al. (2012) use a dust mass absorption coefficient κ_{350} of 0.192 m^2 kg^{-1} at 350 µm whereas da Cunha et al. (2008) assume $\kappa_{850} = 0.077$ m^2 kg^{-1} at 850 µm. Given the scaling relations

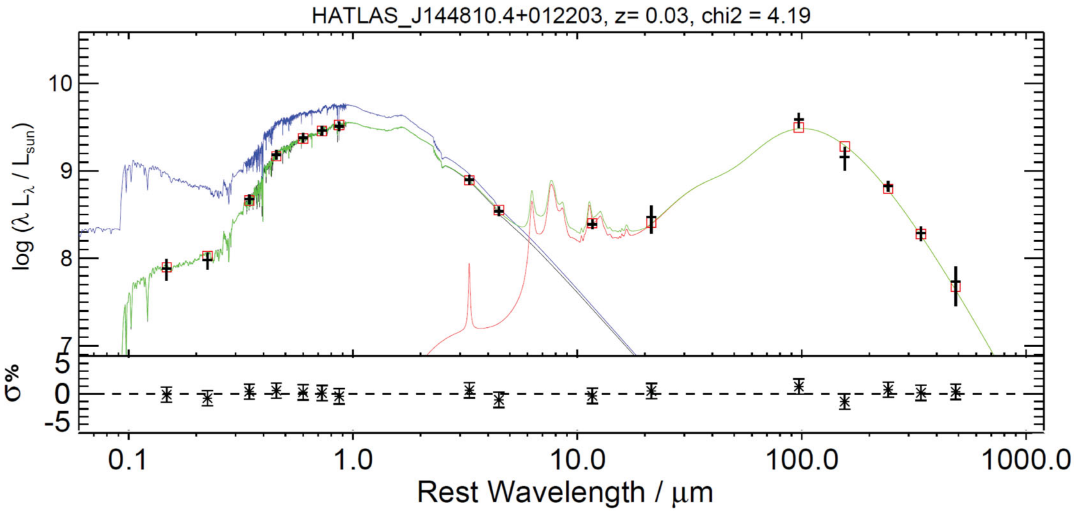

Figure 5. Top panel: a typical MAGPHYS rest-frame SED fit of an H-ATLAS red source. Observed UV to submm fluxes are shown with plus symbols. The green line is the best-fitting model, while the blue line is the unattenuated stellar fitted spectrum. Bottom panel: the fit residuals σ in per cent estimated according to $(L_\lambda^{\rm obs} - L_\lambda^{\rm model})/L_\lambda^{\rm obs}$, where $L_\lambda^{\rm obs}$ and $L_\lambda^{\rm model}$ are the observed and model fluxes in a given photometric band.

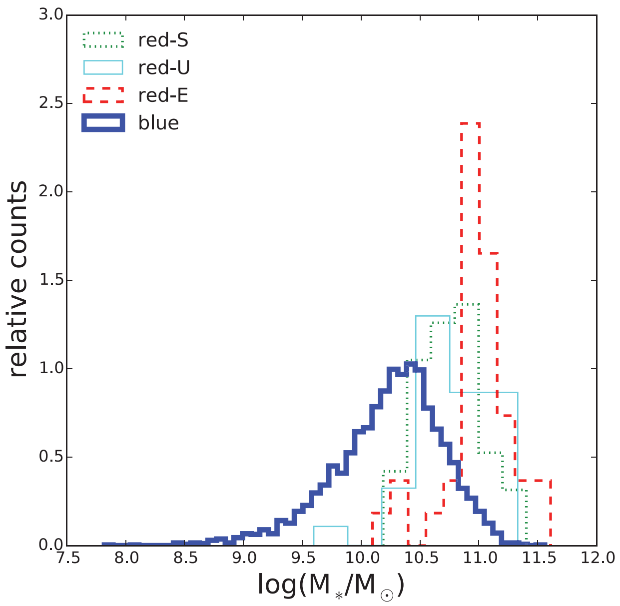

Figure 6. Distribution of galaxy stellar masses in blue (thin solid line) and red samples (*red*-S: dashed line, *red*-U: dotted line, *red*-E: thick solid line). Each histogram is normalized by its integral.

$M_{\rm D} \propto \kappa_\nu^{-1}$ and $\kappa_\nu \propto \nu^{-\beta}$ one finds that κ_{850} in MAGPHYS can be scaled down (assuming $\beta = 2.0$) to 0.45 m^2 kg^{-1} at 350 µm and that dust masses as measured by Cortese et al. (2012) are ≈2.36 times larger than those estimated by MAGPHYS. Thus in Fig. 7, the HRS sample are scaled down for ≈0.37 dex to account for the differences between the two measurements of dust masses.

It can be seen that the $M_{\rm D}/M_*$ ratios for both the *blue* or *red* galaxies agrees reasonably well with estimates from the HRS-detected objects. Furthermore, the *red* sources of type E exhibit, on average, $M_{\rm D}/M_*$ ratios that are noticeably lower than those of *blue* galaxies. This is even more clear in the right-hand panel of Fig. 8 which displays the distributions $M_{\rm D}/M_*$ in all sources. The mean values as summarized in Table 2 suggest that the *red*-E objects have values of the dust-to-stellar masses that are approximately an order of magnitude lower than those in the *blue* sources. This is partly because the *red*-Es have high stellar masses but as is visible in the left-hand panel of Fig. 8, they also have a lower dust content in comparison to the *red*-S and *blue* systems. Note that the distribution of specific dust mass of the *red*-S galaxies does not match the distribution of the *blue* star-forming galaxies. We will discuss this further in Section 3.5.

Table 1. The results of a KS test (*p* values) associated with parameter distributions shown in Figs 3, 4, 6, 8 and 10. We highlight with bold face fonts those parameters for which the KS test indicates a significant difference in the underlying distributions, i.e. $p < 0.001$.

Parameter	*blue* versus *red*-E	*blue* versus *red*-S	*blue* versus *red*-U	*red*-E versus *red*-S	*red*-E versus *red*-U	*red*-S versus *red*-U
Sérsic index	**<0.001**	**<0.001**	**<0.001**	**<0.001**	0.098	0.056
Ellipticity	**<0.001**	0.40	0.0045	**<0.001**	0.013	**<0.001**
$\log(\Sigma_5)$	0.25	0.43	0.13	0.71	0.46	0.63
$\log(M_*/{\rm M}_\odot)$	**<0.001**	**<0.001**	**<0.001**	**<0.001**	**<0.001**	0.94
$\log({\rm SFR})[{\rm M}_\odot {\rm yr}^{-1}]$	**<0.001**	**<0.001**	**<0.001**	0.021	0.87	0.032
$\log({\rm SFR}/M_*)[{\rm yr}^{-1}]$	**<0.001**	**<0.001**	**<0.001**	**<0.001**	0.10	0.012
$\log(M_{\rm D}/{\rm M}_\odot)$	0.50	0.0049	0.0021	0.029	0.89	0.23
$\log(M_{\rm D}/M_*)$	**<0.001**	**<0.001**	**<0.001**	**<0.001**	0.014	0.012
f_μ	**<0.001**	**<0.001**	**<0.001**	0.056	0.87	0.45

Table 2. Mean values of various MAGPHYS output parameters estimated from distributions shown in Figs 8 and 10.

Galaxy type	log (SFR)[$M_\odot yr^{-1}$]	log (SFR/M_*)[yr^{-1}]	log ($M_D/M_\odot$)	log ($M_*/M_\odot$)	log (M_D/M_*)	f_μ
blue	0.43 ± 0.57	− 9.72 ± 0.80	7.84 ± 0.54	10.42 ± 0.47	− 2.58 ± 0.62	0.55 ± 0.53
red (type-S)	− 0.29 ± 0.54	− 11.11 ± 0.65	7.74 ± 0.44	10.86 ± 0.37	− 3.12 ± 0.51	0.88 ± 0.31
red (type-U)	− 0.71 ± 0.53	− 11.34 ± 0.53	7.67 ± 0.39	10.83 ± 0.29	− 3.16 ± 0.44	0.88 ± 0.22
red (type-E)	− 0.67 ± 0.63	− 11.70 ± 0.62	7.62 ± 0.49	11.06 ± 0.26	− 3.44 ± 0.51	0.92 ± 0.29

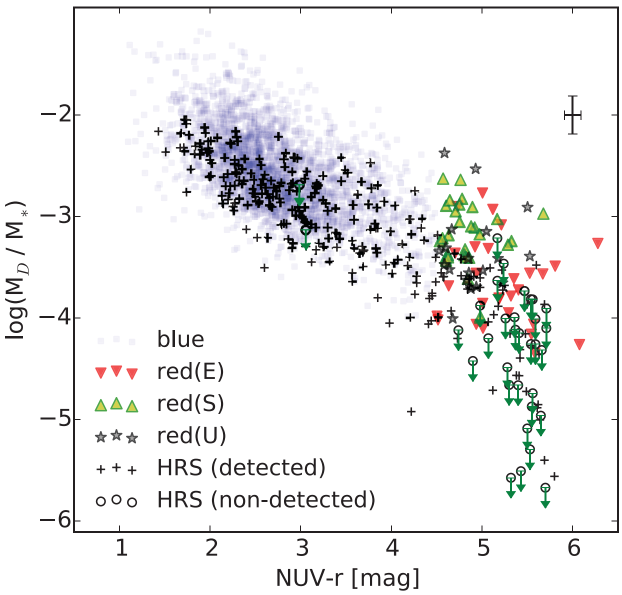

Figure 7. The dust-to-stellar mass ratio as function of NUV−*r*colour for the blue (square) and red samples. E (triangle down), S (triangle up) and U (stars) labels represent the morphology of individual red source. The typical errors associated with our galaxies are indicated on the top-right corner. Overlaid are HRS (*Herschel* Reference Survey; Cortese et al. 2012) detected (plus sign) and non-detected (open circle; downward arrows indicating upper limits) galaxies.

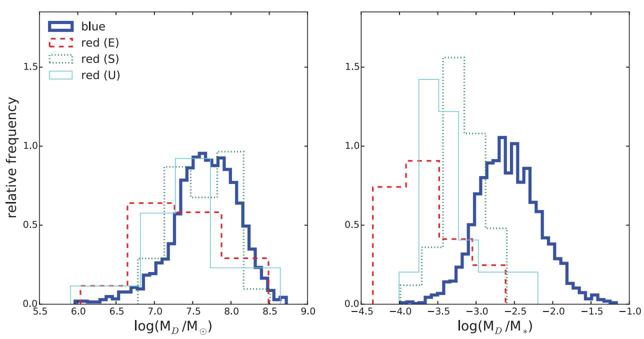

Figure 8. Distributions of dust mass (left-hand panel) as well as specific dust mass (right-hand panel) in the blue (thick solid line) and red sources. E (red dashed line), S (green dotted line) and U (cyan line) labels represent the morphology of individual red source. Each histogram is normalized by its integral. The estimated mean value associated with each histogram is given in Table 2.

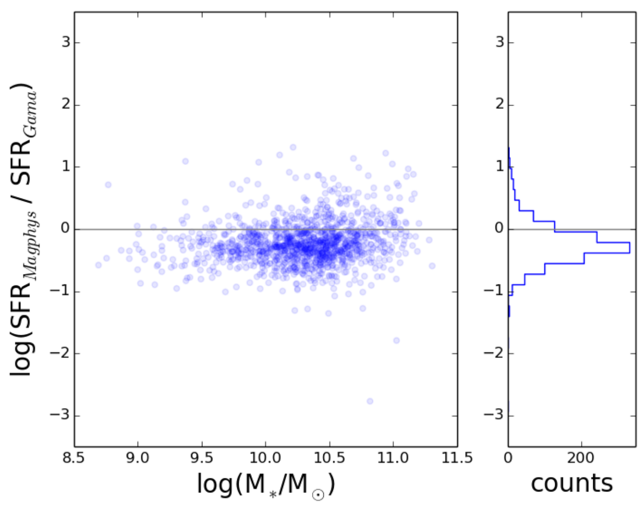

Figure 9. Ratio of MAGPHYS SFR over GAMA DR2 SFR in logarithmic scale versus M_* for all galaxies in our sample (see equation 4). Vertical histogram shows the distributions of data points along *y*-axis.

3.5 Star formation rates

In Fig. 9, we compare the MAGPHYS derived values of the SFRs to those estimated based on the spectral analysis of the Hα lines using the Second GAMA Data Release (GAMA-DR2) catalogues (Wijesinghe et al. 2012; Gunawardhana et al. 2013; Hopkins et al. 2013; Liske et al. 2015).

Galaxy SFRs in GAMA-DR2 are determined from the Kennicutt (1998) relation and based on the total aperture-corrected Hα luminosities observed through fibre spectroscopy. The *r*-band absolute magnitude of each galaxy have been used in order to correct for the aperture and therefore recovering the total Hα luminosities (Hopkins et al. 2003; Gunawardhana et al. 2011). Dust corrections were estimated for each galaxy from the observed Balmer decrement. Finally, stellar absorption corrections were applied to both Hα and H β fluxes which together with the Hα equivalent width allow us to calculate the total aperture-corrected Hα luminosities as described in detail in Hopkins et al. (2003).

We find a strong correlation between the two estimates of SFRs such that (SFRs are in units of $M_\odot$ yr^{-1})

$$\log \mathrm{SFR}_{\mathrm{Magphys}} = 1.22^{+0.02}_{-0.02} \times \log \mathrm{SFR}_{\mathrm{GamaDR2}} - 0.35. \quad (4)$$

Give the Pearson correlation coefficient of $r \simeq 0.71$ in the above equation, it is evident that in general, GAMA DR2 Hα -derived SFRs are well correlated with those predicted by MAGPHYS through SED based measurements though on average MAGPHYS derived SFRs are ≈0.3 dex lower than those based on the Hα luminosities from GAMA. This may be due to different treatments applied in correcting for dust or aperture as explained in Wijesinghe et al. (2011).

The distribution of SFR related parameters are displayed in Fig. 10. The first two panels, show the SFR and the specific star formation rate (SSFR) of *blue* and *red* galaxies. The mean value of the SFR in the *red*-E galaxies is an order of magnitude lower than in the *blue* galaxies with $\mathrm{SFR_{blue}/SFR_{red\text{-}E}} \approx 13$ ($\mathrm{SFR_{red\text{-}S}/SFR_{red\text{-}E}} \approx$ 2.5 ; see also Table 2).

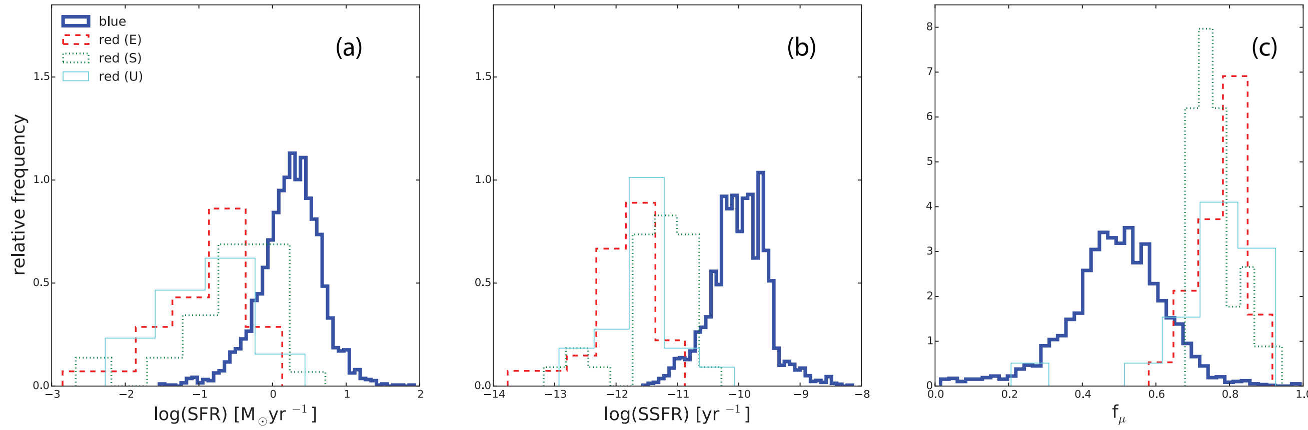

Figure 10. Distributions of (a) SFR, (b) SSFR and (c) f_μ, e.g. the fraction of total dust luminosity contributed by the diffuse ISM, in the blue (thick solid line) and the red sources. E (red dashed line), S (green dotted line) and U (cyan line) labels represent the morphology of individual red source. Each histogram is normalized by its integral. The estimated mean value associated with each histogram is given in Table 2.

The difference between the two samples is even more pronounced when considering SFR normalized by galaxy's stellar mass M_* such that $\mathrm{SSFR_{blue}/SSFR_{red\text{-}E}} \approx 100$ ($\mathrm{SSFR_{red\text{-}S}/SSFR_{red\text{-}E}} \approx 4$). For both the SFR and the SSFR, the values estimated for the *red*-S-type sources and the galaxies with uncertain morphology, lay between the *red*-E galaxies and the *blue* control sample. In comparison, Rowlands et al. (2012, i.e. table C1) measure $-9.99^{+0.03}_{-0.03}$ and $-10.85^{+0.14}_{-0.14}$ for SSFR in samples of 'H-ATLAS spiral' and 'H-ATLAS elliptical' galaxies, respectively.

Fig. 10(c) shows the normalized distributions of f_μ in the *blue* and *red* populations. The *red*-E galaxies have an average $f_\mu \sim 0.92$, well above the mean (∼0.55) of the *blue* galaxies. This indicates that while about half of the observed FIR emission observed in the *blue* galaxies comes from dust in birth clouds, the FIR of *red*-E galaxies is dominated by dust in the diffuse ISM. We note that the average derived f_μ for the *red*-S systems is significantly higher than for the *blue* control sample and only slightly lower than for the sample of the *red*-E galaxies.

3.5.1 *On the derived properties of the red-S sample*

Even though the *red*-S galaxies are not the prime focus of this paper, this sample does display some interesting characteristics that are worth commenting on briefly. As can be derived from Figs 6, 8(b) and 10 the deduced properties of the *red*-S galaxies do not match the *blue* galaxy properties. The *red*-S galaxies appear intermediate between the *red*-E and the *blue* galaxies in stellar mass, SFR and specific dust mass. This offset is primarily driven by the higher derived stellar masses and the correspondingly lower SFR. This is contrary to what one would expected if the red colours of the edge-on galaxies are *only* due to their high inclination.

Inclination does play a significant role in defining this sample, as can be concluded from Fig. 11. We show in this figure the inclination of the *blue* + *red*-S for the stellar masses above $\log(M_*/\mathrm{M}_\odot) \approx 10.0$, i.e. the range of stellar masses of interest. There is a definite trend of the median inclination against observed optical redness and in particular the very reddest sources are almost exclusively very inclined sources.

We see two main interpretations – which could be at play simultaneously – that could explain these characteristics of the *red*-S sample.

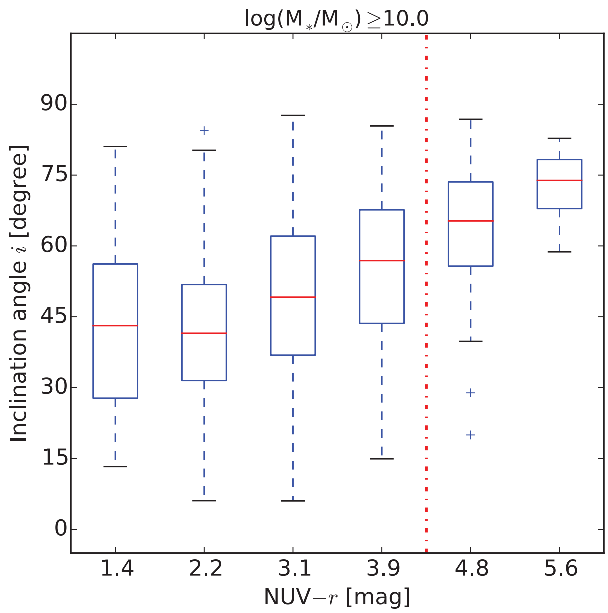

Figure 11. Distribution of galactic inclination angles i for *blue* and *red*-S galaxies, having stellar masses $\log(M_*/\mathrm{M}_\odot) \geq 10.0$, versus NUV$-r$ colour. Each box extends from the lower to upper quartile values of data, with a line at the median (red line). Inclination angles are computed using equation (2). Dashed lines extending vertically from the boxes indicating variability outside the upper and lower quartiles. Individual data points indicate outliers. The vertical dash–dotted line intersects the x-axis at NUV$-r = 4.5$ above which galaxies are classified as red.

(i) High inclination is a necessary, but not sufficient condition for a star-forming disc galaxy to be submm detected *and* very optically red. In this case, the red colour would apparently select preferentially the more massive disc galaxies. Perhaps the less massive disc galaxies have enough star formation in their periphery of their discs – which would not be strongly obscured, even in the case of strong inclination – to exhibit a blueish optical colour. Alternatively, the red colour of those massive discs could be a direct results of a dominant old stellar population.

(ii) The galaxy parameters, derived from MAGPHYS, of the very inclined and dusty sources are systematically biased to higher stellar masses and less star formation. This is in line with the finding of da Cunha et al. (2010). These authors find that the derived SFR for edge-on galaxies is about a factor of 3× (≈0.48 dex) below their face-on counterparts. They also find that this effect is also responsible for the lower dust masses (or dust luminosities) and higher f_μ estimated for edge-on in comparison to face-on galaxies. The amplitude of this effect is insufficient to directly explain the difference we find between the blue sample and the *red*-S sample. Note however that da Cunha et al. (2010) describe the effect on an *inclined* sample of galaxies while the *red*-S sample is selected to have only galaxies with very red colours. The *inclined* sample contains galaxies with varying degrees of hidden star formation, whereas the *red*-S sample contains only galaxies with very obscured star formation. We thus would expect to find a larger offset of the derived parameters in the *red*-S sample than in the *inclined* sample.

Clearly this red disc population of nearby galaxies deserves further attention in a dedicated study.

3.6 Dust mass correlations with galactic properties

We show in Fig. 12 correlation plots of the derived dust mass versus a number of key parameters (M_*, SFR and f_μ) in the *red*-E and *blue* galaxies. These parameters have been chosen to elucidate the possible origin and role of the dust in the *red*-E galaxies. The first conclusion that can be drawn from the perusal of these diagrams is that the *red*-E galaxies clearly occupy a different parameter space from *blue* spiral galaxies.

Fig. 12(a) shows a very different behaviour of the $M_{\rm D}$ as a function of M_* for the blue galaxies and the *red*-E sample. The blue sample shows a roughly linear correlation (with scatter) between the dust reservoir and the M_*. This relation is expected due to the M_*–SFR relation for normal galaxies, if the $M_{\rm D}$ is measuring the reservoir available for star formation. The *red*-E sample exhibits a totally different behaviour apart from being located in a distinctly different part of this diagram. While the host galaxies are all – with one outlier – of very similar mass ($\approx 10^{11} {\rm M}_\odot$) their dust content spans more than two orders of magnitude. This complete decorrelation of stellar mass and dust content argues against a stellar origin (e.g. Cortese et al. 2012) for the dust in those galaxies. While for blue galaxies the dust mass increases with stellar mass, the dust masses found for the *red*-E span ≈2 order of magnitudes for stellar masses that are roughly constant at $\approx 10^{11}\ {\rm M}_\odot$ (see Table 3).

In Fig. 12(b), we show that there *is* a moderate correlation in the *red*-E galaxies between the derived SFR and $M_{\rm D}$ with a similar slope but offset from the *blue* sequence. We interpret the existence of this correlation as an indication that the star formation is probably taking place in the cold gas associated with the dust.

The observed offset between the *blue* control sample and the *red*-E sample implies that the same amount of dust in the *red*-E galaxies is associated with about an order of magnitude less star formation. This could be an indication that the physical state of the cold ISM phase in the *red*-E galaxies is significantly different perhaps due to the very different environment in which the cold gas is embedded. This interpretation is corroborated by Fig. 12(c) where we show that indeed the MAGPHYS derived fraction of the dust heating due to the interstellar radiation field, i.e. f_μ is much higher in the *red*-E galaxies than their *blue* counterparts.

3.7 The origin of dust in *red*-E

In the classical definition of galactic types, ellipticals were classified as devoid of gas and dust (Hubble 1926; de Vaucouleurs 1959;

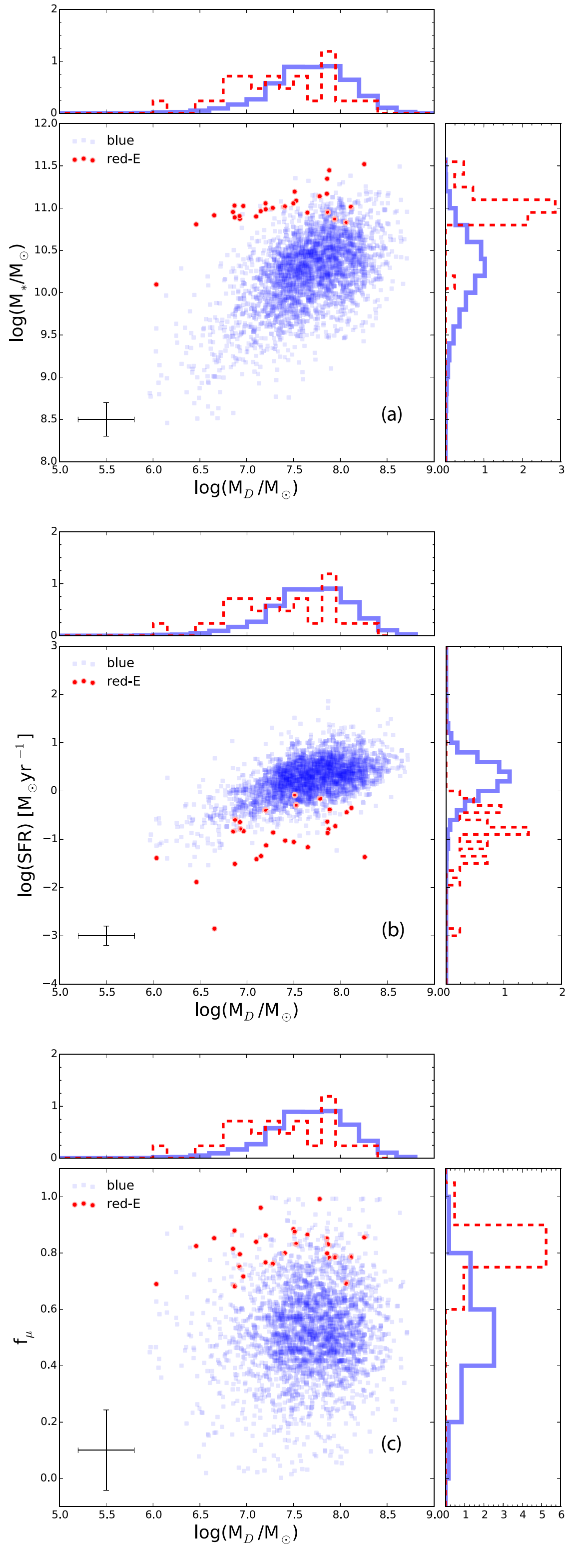

Figure 12. Distribution of dust mass $M_{\rm D}$ against (a) stellar mass M_* (b) star formation rate, SFR and (c) f_μ in *blue* (blue square), *red*-E (red circle). In addition, horizontal and vertical histograms show the distributions of data points along *x*- and *y*-axes with blue/thick and red/dashed lines representing *blue* and *red*-E. Each histogram is normalized by its integral. Typical errors associated with various parameters are indicated on the bottom-left corner. Results of linear regression analysis to *blue* and *red*-E observed data points in panels 'a' and 'b' are given in Table 3.

Table 3. Results of linear regression analysis to the observed data points in panels 'a' and 'b' of Fig. 12. Parameters in the table are associated with the linear model $Y = s(\pm \mathrm{err}) \times X + c$.

Galaxy type	Y	X	s (slope)	± err (standard deviation)	c (intercept)	r value (Pearson correlation)	p value
blue (panel a)	$\log(M_*/\mathrm{M}_\odot)$	$\log(M_\mathrm{D}/\mathrm{M}_\odot)$	0.56	0.01	5.93	0.54	<0.001
red-E (panel a)	–	–	0.30	0.06	8.76	0.67	<0.001
blue (panel b)	$\log(\mathrm{SFR})\ [\mathrm{M}_\odot\,\mathrm{yr}^{-1}]$	$\log(M_\mathrm{D}/\mathrm{M}_\odot)$	0.54	0.01	– 3.89	0.56	<0.001
red-E (panel b)	–	–	0.54	0.18	– 4.87	0.50	0.006

Sandage 1961). In the subsequent years, dust emission in ellipticals has been detected from the ground (Hawarden et al. 1981; Sadler & Gerhard 1985; Sparks et al. 1985; Kormendy & Stauffer 1987; Ebneter, Djorgovski & Davis 1988; Pandey et al. 2001) and from space using the *Infrared Astronomical Satellite* (Jura et al. 1987; Knapp et al. 1989) and the *Spitzer Space Telescope* (Rocca-Volmerange et al. 2007). Dust lanes were observed early on along the minor axis of ellipticals (Bertola & Galleta 1978). When in some ellipticals the dust lanes and stars were observed to rotate in opposite direction, this was suggestive that this dust must have been accreted and cannot be accounted for by mass-loss from evolved stars (Kormendy & Djorgovski 1989). Kinematic information is important in order to constrain the presence of counter-rotating gas (and dust) in ellipticals in order to establish the frequency of the accretion scenario (Bertola, Buson & Zeilinger 1988).

In this study, the unresolved red ellipticals detected in the submm do not have associated kinematic information. However, we attempt to establish whether the present dust masses in our sample of elliptical galaxies can be explained with stellar sources using a model of dust formation and evolution in ellipticals. We compare the specific dust masses (M_D/M_*) with the predictions for dust mass return from a single stellar population (SSP) model and which represents an instantaneous burst of star formation. The star formation histories of the observed galaxies are more complex than that represented by a single burst of star formation. Their stellar masses and colours are however clearly dominated by the old stellar populations. Moreover, chemical evolution models of elliptical galaxies find very short time-scales of their formation and high star formation efficiencies of the initial starburst (Pipino et al. 2005). The present SFR of $\sim$0.1 $\mathrm{M}_\odot\,\mathrm{yr}^{-1}$ in our sample is several orders of magnitude lower than that the SFR in the past responsible for the build-up of their stellar mass of $\sim10^{11}$ $\mathrm{M}_\odot$. Therefore, for comparison with the dust model predictions, we assume that the entire stellar mass of each red-E galaxy is associated with a single burst with an age equal to its mass weighted age derived from the SED fitting. The observed dust mass in a galaxy is thus compared with the survived dust mass from the SSP with the same age. The model of the SSP adopted here was introduced in Zhukovska (2008) and was used to describe the chemical evolution of dust and gas in the Milky Way and dwarf galaxies (Zhukovska, Gail & Trieloff 2008; Zhukovska 2014). For the chemical evolution aspects of the SSP model, we adopt the same ingredients as in Zhukovska (2008) except for the IMF, for which we use the Chabrier (2003) form. This is consistent with the IMF that is adopted in the SED fitting with MAGPHYS.

The model includes dust production by Type II supernovae (SNe) and by asymptotic giant branch (AGB) stars. Type Ia SNe are an important source of metallic iron in early-type galaxies. Models of dust evolution imply that, with an assumption of high-condensation efficiencies of metals into dust in their ejecta, they can dominate dust input in elliptical galaxies (e.g. Calura, Pipino & Matteucci 2008; Pipino et al. 2011). FIR observational surveys of both warm and cool dust in remnants of Type Ia SNe do not however find evidence of efficient dust formation, in contrast to remnants of Type II SNe (Gomez et al. 2012). This is supported by theoretical models, which indicate that newly formed grains are small and are easily destroyed in shocked gas before being ejected into the ISM (Nozawa et al. 2011). Therefore, we neglect the dust input from Type Ia SNe.

The net input from Type II SNe is still debated. We add their contribution for completeness, as they produce dust for a limited period of time after stars have formed ($\sim$40 Myr). We adopt relatively low efficiencies of dust condensation in the SNe ejecta. These are constrained by meteoritic data and the observed metallicity–dust to gas ratio relation in dwarf galaxies (Zhukovska et al. 2008; Zhukovska 2014).

The mass- and metallicity-dependent dust yields for AGB stars are taken from the work of Ferrarotti & Gail (2006) with additional models from Zhukovska et al. (2008). These dust yields were computed for stellar metallicity ranging from $Z = 0.001$ up to the suprasolar values of 0.04 and for the stellar mass range [1–7] $\mathrm{M}_\odot$. We extrapolate the dust yields in the mass range [7–8] $\mathrm{M}_\odot$. Only one galaxy in the red-E sample is old enough for stars with masses below 1 $\mathrm{M}_\odot$ to contribute to the dust budget. However, stars in this mass range lose a large fraction of their envelopes during red giant branch evolution characterized by inefficient dust formation (Gail et al. 2009; McDonald et al. 2011a, 2015). Some amount of dust is condensed during following AGB stage, but the total dust mass returned to the ISM is very low. Estimates based on the gas mass-loss rates derived in McDonald et al. (2011b) and McDonald et al. (2015) point to $\lesssim10^{-3}$ $\mathrm{M}_\odot$ of dust per star. Given this low value, we choose not to extrapolate the dust yields down to 0.8 $\mathrm{M}_\odot$ and neglect dust input from these stars.

The ISM in elliptical galaxies is dominated by hot rarefied gas with temperatures of $\sim10^7$ K (Mathews & Brighenti 2003). Grains can be rapidly sputtered in high-temperature gas due to collisions with ions (mostly with abundant H^+; Draine & Salpeter 1979; Itoh 1989). The time-scale of destruction by thermal sputtering can be approximated as

$$\tau_\mathrm{sput} = 10^5 \left(1 + (10^6\,\mathrm{K}/T)^3\right) \frac{a/0.1\,\mu\mathrm{m}}{n/\mathrm{cm}^{-3}}\ \mathrm{yr}, \tag{5}$$

where n and T are the number density and temperature of the hot gas, respectively, and a is the grain radius. The total stardust mass $M_\mathrm{D}(t)$ is reduced by thermal sputtering in the hot gas at the rate

$$\frac{\mathrm{d}M_\mathrm{D}(t)}{\mathrm{d}t} = -\frac{M_D(\mathrm{t})}{\tau_\mathrm{sput}}. \tag{6}$$

The temperature and density of the hot gas are derived from observations of extended X-ray emission. For simplicity, we assume single values for the electron density and temperature of the gas of 10^{-3} cm^{-3} and 1.5 × 10^7 K, respectively (Mathews & Brighenti 2003) resulting in τ_sput =100 Myr. Note that τ_sput depends only weakly on temperature in the regime appropriate for the hot ISM of

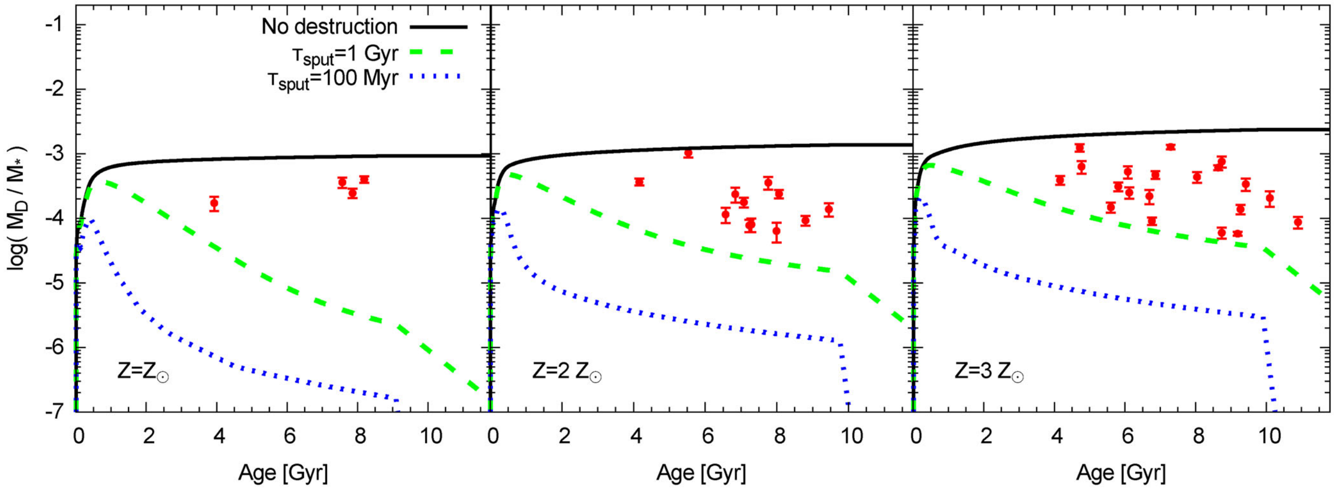

Figure 13. The evolution of the dust mass relatively to the stellar mass of as a function of the age of SSP. The left-hand, middle and right-hand panel indicate initial metallicities of $Z = 1$, 2 and 3 $Z_{\odot}$, respectively. The value of the solar metallicity adopted here is $Z_{\odot} = 0.014$ (Asplund et al. 2009). The solid lines show the evolution of the cumulative dust mass returned in the SSP. The evolution of dust mass for the same SSP model with dust destruction by thermal sputtering on the time-scales of 1 Gyr and 100 Myr are shown with the dashed and dotted lines, respectively. The filled red circles represent the sample of *red*-E galaxies which have been grouped in metallicity bins of [0.5–1.5], [1.5–2.5] and >2.5 $Z_{\odot}$. The specific dust masses of each *red*-E galaxy in the sample is plotted versus the mass weighted age of its stellar populations and the metallicity of each galaxy is obtained from the SDSS DR4 (Gallazi et al. 2005).

elliptical galaxies and a value of $T = 10^6$ K results in the time-scale of 200 Myr. A similarly low value of the time-scale of interstellar dust destruction, only 46 Myr, is derived for early type galaxies (ETGs) detected in FIR by *Spitzer* observations (Clemens et al. 2010). For a comparison, we also ran calculations of the SSP evolution with a longer dust destruction time-scale of 1 Gyr which corresponds to a lower gas density of 10^{-4} cm^{-3}. This long time-scale may also account for the fact that many early-type galaxies may harbour cold gas (Mathews & Brighenti 2003; Alatalo et al. 2013; Young et al. 2014), where grains are protected for some time from the thermal sputtering and can survive longer. Another mechanism of dust destruction is inertial sputtering in SN shocks, which is thought to be the dominant mechanism of dust destruction in spiral galaxies. However, in a hot rarefied medium one SN destroys 20 times less dust compared to the local ISM conditions (McKee 1989). We therefore do not consider dust destruction by Type Ia SNe and restrict our consideration to the thermal sputtering in hot gas. Dust mass in an early-type galaxy can also be substantially reduced by the galactic winds (not considered in the present model). Our estimates should therefore be considered as the upper limit for the stardust mass.

Fig. 13 compares the specific dust masses we have derived for the sample of *red*-E to the results of the SSP models.[4] The data are grouped in three metallicity bins of [0.5–1.5], [1.5–2.5] and >2.5 $Z_{\odot}$ and compared to three sets of SSP models with $Z = Z_{\odot}$ (left-hand panel), $Z = 2\,Z_{\odot}$ (middle panel), and $Z = 3\,Z_{\odot}$ (right-hand panel). The specific dust masses of each *red*-E galaxy in the sample is plotted versus the mass weighted age of its stellar populations and the metallicity of each galaxy is obtained from the SDSS DR4 (Gallazi et al. 2005). The figure clearly shows that, as expected, SSP models with no dust destruction tend to overpredict the amount of dust in these ellipticals. On the other hand, more realistic models with dust sputtering fail to reproduce the observed $M_{\rm D}/M_*$ ratio even when a relatively long dust destruction time-scale of 1 Gyr is considered. The SSP models with dust destruction underpredicts the ratio of $M_{\rm D}/M_*$ by more than two order of magnitude. These estimates demonstrate that dust return into ISM from stellar sources is not sufficient to explain the observed $M_{\rm D}/M_*$. This implies an external origin of the dust via minor mergers and/or efficient dust growth in the dense ISM.

The amount of dust in the submm-detected galaxies as well as its correlation with the present-day SFR (Fig. 12, panel b) suggests a connection between the dust and the dense ISM in agreement with Alatalo et al. (2013), who find that the distribution of the CO and dust in nearby ETG is spatially correlated. The time-scale for dust growth in molecular clouds is short and of the order of a few to several 10^7 yr (Hirashita 2000). We estimate an upper bound on the dust mass that may result from dust growth in the dense ISM in the following manner. Assuming a specific mass of molecular gas $M_{\rm H_2}/M_{\star}$ of 0.01 and a value of 0.06 for the specific mass of the atomic gas $M_{\rm H\,I}/M_{\star}$ (these are the observed upper limits in Young et al. 2014), a dust-to-hydrogen mass ratio of 0.018 (i.e. about 3 times the solar value), and a complete condensation of heavy elements into dust in the molecular gas, this yields a specific dust mass $M_{\rm D}/M_{\star}$ of $0.07 \times 0.018 \approx 1.3 \times 10^{-3}$ which is only slightly higher than the largest specific dust masses measured for the sample of red ellipticals that are displayed in Fig. 13. This means that it is difficult, but not impossible, to explain the measured dust masses as resulting from grain growth in the dense gas inside the elliptical galaxies. It should be noted that dust growth does not preclude the role of minor mergers because the molecular gas may have an external origin (Davis et al. 2011).

4 CONCLUSIONS

In this work, we examine the properties of low-redshift galaxies detected in 250 μm(>5σ) using H-ATLAS DR1 catalogue. We define two sub-samples of *red* and *blue* galaxies based on NUV$-r$ colours. Our aim is to understand the nature of the *red* subset in comparison to those in the *blue* sub-sample. We can summarize our findings as follows.

[4] Value of the solar metallicity adopted here is $Z_{\odot} = 0.014$ (Asplund et al. 2009).

(i) Within the redshift range $0.01 \leq z \leq 0.2$ of our sample, *red* sources with the UV-optical colour indices of NUV$-r \geq 4.5$, constitute ≈4.2 per cent of the total number of systems in H-ATLAS. The fraction of *red* sources increases with the galaxy stellar mass such that in $\gtrsim$97 per cent of the *red* sample, $M_* \gtrsim 10^{10}$ M$_\odot$.

(ii) Following the visual inspection of galaxies, sources in the *red* sample were grouped into three categories of elliptical (E), spiral (S) and uncertain (U). We find that at least $\gtrsim$30 per cent of the *red* sources are of type E and more than $\gtrsim$40 per cent of sources belong to type S.

(iii) Both *blue* and *red* sources, seem to occupy environments with similar densities (e.g. having similar $\log(\Sigma_5)$ distributions) though in comparison to *blue* and *red* objects of type S and U, a slightly larger fraction of *red*-E sources are in relatively denser regions with $\log(\Sigma_5/\mathrm{Mpc}^{-2}) \gtrsim 1.5$.

(iv) The SED analysis of galaxies in our sample based on MAGPHYS, reveals that the *red* galaxies (either type S or E) span a similar range of dust masses but different dust-to-stellar mass ratios in comparison to the *blue* galaxies. The specific dust masses in the *blue* and *red*-S galaxies are, on average, larger than those found for the *red*-E sample by a factor of 7× and 2×, respectively. Similarly, galaxies of type E have lower levels of mean SFR and SSFR in contrast to sources in the *blue* and *red*-S samples. Furthermore, analysis of f_μ shows that unlike *blue* galaxies where star-forming regions have the main contribution to the observed submm fluxes, FIR emission in the *red* systems of type E is mainly from the dust in the ISM.

(v) The UV-optical colours of the *red*-S sample could be the result of their highly inclined orientation and/or a strong contribution of the old stellar population. However, in the current work we did not further investigate the contribution of each factor to the observed colour of the *red*-S sources.

(vi) Finally, the comparison of specific dust masses (M_D/M_*) of the *red* elliptical galaxies to the dust evolution in SSP models excludes that the origin of the dust is from internal stellar sources. Dust growth in molecular clouds and/or gas and dust accretion through minor mergers provide more realistic and appealing alternatives (e.g. Gomez et al. 2010; Smith et al. 2012b).

Our results show that there exist a population of early-type galaxies, containing a significant level of cold dust similar to those observed in blue/star-forming galaxies. The origin of dust in such early-type galaxies is likely to be of external origin (e.g. fuelled through mergers and tidal interactions). Hence, it is interesting to know the difference between *red* galaxies which are detected in 250µm and those without any submm detection in the hope to find the mechanisms that are responsible for tuning the dust content in passive and/or early-type galaxies.

ACKNOWLEDGEMENTS

We would like to thank the anonymous referee for his valuable comments and suggestions which helped to improve this paper.

SD is supported by a Marie-Curie Intra European Fellowship under the European Community's Seventh Framework Programme FP7/2007-2013 grant agreement no. 627008. SH acknowledges support from the *Deutsche Forschungsgemeinschaft* (DFG) in the collaborative research project SFB881 The Milky Way System (subprojects B1). RJI, LD and SJM acknowledge support from the European Research Council Advanced Grant, cosmicism. SZ acknowledge support by the Deutsche Forschungsgemeinschaft through SPP 1573: Physics of the Interstellar Medium. GdZ acknowledge financial support from ASI/INAF Agreement 2014-024-R.0 for the *Planck* LFI activity of Phase E2. KR acknowledges support from the European Research Council Starting Grant SEDmorph (P.I: V. Wild).

The *Herschel*-ATLAS is a project with *Herschel*; which is an ESA space observatory with science instruments provided by European-led Principal Investigator consortia and with important participation from NASA. The H-ATLAS website is http://www.h-atlas.org/. GAMA is a joint European-Australasian project based around a spectroscopic campaign using the Anglo-Australian Telescope. The GAMA input catalogue is based on data taken from the SDSS and UKIDSS. Complementary imaging of the GAMA regions is being obtained by a number of independent survey programmes including *GALEX* MIS, VST KIDS, VISTA VIKING, *WISE*, *Herschel*-ATLAS, GMRT and ASKAP providing UV to radio coverage. GAMA is funded by the STFC (UK), the ARC (Australia), the AAO, and the participating institutions. The GAMA website is http://www.gama-survey.org/. MAGPHYS is available via http://www.iap.fr/magphys/magphys/MAGPHYS.html.

REFERENCES

Abazajian K. N. et al., 2009, ApJS, 182, 543
Adelman-McCarthy J. K. et al., 2008, ApJS, 175, 297
Agius N. K. et al., 2013, MNRAS, 431, 1929
Alatalo K. et al., 2013, MNRAS, 432, 1796
Asplund M., Grevesse N., Sauval A. J., Scott P., 2009, ARA&A, 47, 481
Auld R. et al., 2013, MNRAS, 428, 1880
Baldry I. K. et al., 2004, ApJ, 600, 681
Ball N. M., Loveday J., Brunner R. J., 2008, MNRAS, 383, 907
Balogh M., Baldry I. K., Nichol R., Miller C., Bower R., Glazebrook K., 2004, ApJ, 615, L101
Barden M. et al., 2005, ApJ, 635, 959
Bell E. F. et al., 2004a, ApJ, 600, 11
Bell E. F. et al., 2004b, ApJ, 608, 752
Bendo G. J. et al., 2012, MNRAS 419, 1833
Bertola F., Galletta G., 1978, ApJ, 226, L115
Bertola F., Buson L. M., Zeilinger W. W., 1988, Nature, 335, 705
Binggeli B., Tammann G. A., Sandage A., 1987, AJ, 94, 251
Boselli A. et al., 2010, PASP, 122, 261
Bourne N. et al., 2012, MNRAS, 421, 3027
Brough S. et al., 2013, MNRAS, 435, 2903
Bruzual G., Charlot S., 2003, MNRAS, 344, 1000
Burgarella D., Buat V., Iglesias-Pàramo J., 2005, MNRAS, 360, 1413
Butcher H., Oemler A., Jr, 1984, ApJ, 285, 426
Calura F., Pipino A., Matteucci F., 2008, A&A, 479, 669
Chabrier G., 2003, PASP, 115, 763
Charlot S., Fall S. M., 2000, ApJ, 539, 718
Clemens M. S., Jones A. P., Bressan A., Baes M., Bendo G. J., 2010, A&A, 518, L50
Cluver M. E. et al., 2014, ApJ, 782, 90
Condon J. J. et al., 1998, AJ, 115, 1693
Conroy C., Gunn J. E., White M., 2009, ApJ, 699, 486
Conselice C. J., 2014, ARA&A, 52 291
Cooper M. C. et al., 2006, MNRAS, 370, 198
Cortese L., 2012, A&A, 543, 132
Cortese L., Boselli A., Franzetti P., Decarli R., Gavazzi G., Boissier S., Buat V., 2008, MNRAS, 386, 1157
Cortese L. et al., 2012, A&A, 540, 52
Croton D. J. et al., 2006, MNRAS, 365, 11
Cucciati O. et al., 2006, A&A, 458, 39
da Cunha E., Charlot S., Elbaz D., 2008, MNRAS, 388, 1595
da Cunha E., Eminian C., Charlot S., Blaizot J., 2010, MNRAS, 403, 1894
Dale D. A. et al., 2007, ApJ 655, 863
Dale D. A. et al., 2012, ApJ 745, 95
Dariush A. et al., 2011, MNRAS, 418, 64
Davies J. I. et al., 2010, A&A 518, L48

Davis T. A., Alatalo K., Sarzi M., Bureau M., Young L. M., 2011, MNRAS, 417, 882
De Looze I. et al., 2010, A&A 518, L54
de Vaucouleurs G., 1959, Handbuch Phys., 53, 275
di Serego Alighieri S. et al., 2013, A&A, 552, 8
Draine B. T., Salpeter E. E., 1979, ApJ, 231, 438
Dressler A., 1980, ApJ, 236, 351
Driver S. P., Liske J., Cross N. J. G., De Propris R., Allen P. D., 2005, MNRAS, 360, 81
Driver S. P., Popescu C. C., Tuffs R. J., Liske J., Graham A. W., Allen P. D., de Propris R., 2007, MNRAS, 379, 1022
Driver S. P. et al., 2009, Astron. Geophys., 50, 12
Driver S. P. et al., 2011, MNRAS, 413, 971
Dunne L., Eales S., 2001, MNRAS, 327, 697
Eales S. et al., 2010, PASP, 122, 499
Ebneter K., Balick B., 1985, AJ, 90, 183
Ebneter K., Djorgovski S., Davis M., 1988, AJ, 95, 422
Ferrarotti A. S., Gail H.-P., 2006, A&A, 447, 553
Gail H., Zhukovska S., Hoppe P., Trieloff M., 2009, ApJ, 698, 1136
Gallazi A., Charlot S., Brinchmann J., White S. D. M., Tremonti C. A., 2005, MNRAS, 362, 41
Gomez H. L. et al., 2010, A&A, 518, 45
Gomez H. L. et al., 2012, MNRAS, 420, 3557
Goudfrooij P., de Jong T., Hansen L., Norgaard-Nielsen H. U., 1994, MNRAS, 271, 833
Grootes M. W. et al., 2013, ApJ, 766, 59
Gunawardhana M. L. P. et al., 2011, MNRAS, 415, 1647
Gunawardhana M. L. P. et al., 2013, MNRAS, 433, 2764
Hawarden T. G., Elson R. A. W., Longmore A. J., Tritton S. B., Corwin H. G., 1981, MNRAS, 196, 747
Hill D. T. et al., 2011, MNRAS, 412, 765
Hirashita H., 2000, PASJ, 52, 585
Hopkins A. M. et al., 2003, ApJ, 599, 971
Hopkins A. M. et al., 2013, MNRAS, 430, 2047
Hubble E., 1926, ApJ, 64, 321
Ibar E. et al., 2010, MNRAS, 409, 38
Itoh H., 1989, PASJ, 41, 853
Jarvis M. J. et al., 2010, MNRAS, 409, 92
Johnson B. D. et al., 2007, ApJS, 173, 377
Jura M., Kim D. W., Knapp G. R., Guhatthakurta P., 1987, ApJ, 312, L11
Kaviraj S. et al., 2007, ApJS, 173, 619
Kennicutt R. C., Jr, 1998, ARA&A, 36, 189
Knapp G. R., Guhathakurta P., Kim D. W., Jura M., 1989, ApJS, 70, 329
Kormendy J., Djorgovski S., 1989, ARA&A, 27, 235
Kormendy J., Stauffer J., 1987, in de Zeeuw T., ed., Proc. IAU Symp. 127, Structure and Dynamics of Elliptical Galaxies. Reidel, Dordrecht, p. 405
Lawrence A. et al., 2007, MNRAS, 379, 1599
Leeuw L. L., Sansom A. E., Robson E. I., Haas M., Kuno N., 2004, ApJ, 612, 837
Lewis I. et al., 2002, MNRAS, 334, 673
Liske J., Lemon D. J., Driver S. P., Cross N. J. G., Couch W. J., 2003, MNRAS, 344, 307
Liske J. et al., 2015, MNRAS, 452, 2087
McDonald I. et al., 2011a, ApJS, 193, 23
McDonald I. et al., 2011b, ApJ, 730, 71
McDonald I. et al., 2015, MNRAS, 448, 502
McKee C., 1989, in Allamadola L. J., Tielens A. G. G. M., eds, the Proceedinfgs of Interstellar Dust, IAU Symposium 135, Kluwer Academic Publishers, Dordrecht, p. 341
Masters K. L. et al., 2010, MNRAS, 405, 783
Mathews W. G., Brighenti F., 2003, ARA&A, 41, 191
Morrissey P. et al., 2005, ApJ, 619, L7
Mulchaey J. S., 2000, ARA&A, 38, 289
Nozawa T., Maeda K., Kozasa T., Tanaka M., Nomoto K., Umeda H., 2011, ApJ, 736, 45
Odenwald S., Newmark J., Smoot G., 1998, ApJ, 500, 554
Pandey S. K., Sahu D. K., Kembhavi A. K., McCarthy P. J., 2001, BASI, 29, 449
Pascale E. et al., 2011, MNRAS, 415, 911
Pilbratt G. et al., 2010, A&A, 518, 1
Pipino A., Kawata D., Gibson B. K., Matteucci F., 2005, A&A, 434, 553
Pipino A., Fan X. L., Matteucci F., Calura F., Silva L., Granato G., Maiolino R., 2011, A&A, 525, 61
Poggianti B. M. et al., 2009, ApJ, 697, 137
Poggianti B. M., De Lucia G., Varela J., Aragon-Salamanca A., Finn R., Desai V., von der Linden A., White S. D. M., 2010, MNRAS, 405, 995
Popescu C. C., Tuffs R. J., 2002, MNRAS, 335, 41
Popescu C. C., Tuffs R. J., Völk H. J., Pierini D., Madore B. F., 2002, ApJ, 567, 221
Ravindranath S. et al., 2004, ApJ, 604, 9
Rigby E. E. et al., 2011, MNRAS, 415, 2336
Rocca-Volmerange B., de Lapparent V., Seymour N., Fioc M., 2007, A&A, 475, 801
Rowlands K. et al., 2012, MNRAS, 419, 2545
Sadler E. M., Gerhard O. E., 1985, MNRAS, 214, 177
Sandage A., 1961, The Hubble Atlas of Galaxies. Carnegie Inst., Washington, DC
Savoy J., Welch G. A., Fich M., 2009, ApJ, 706, 21
Simard L., Mendel J. T., Patton D. R., Ellison S. L., McConnachie A. W., 2011, ApJS, 196, 11
Smith D. J. B. et al., 2011, MNRAS, 416, 857
Smith D. J. B. et al., 2012a, MNRAS, 427, 703
Smith M. W. L. et al., 2012b, ApJ, 748, 123
Sodrosk T. J., Odegard N., Arendt R. G., Dwek E., Weiland J. L., Hauser M. G., Kelsall T., 1997, ApJ, 480, 173
Sparks W. B., Wall J. V., Thorne D. J., Jorden P. R., van Breda I. G., Rudd P. J., Jorgensen H. E., 1985, MNRAS, 217, 87
Strateva I. et al., 2001, AJ, 122, 1861
Sutherland W., Saunders W., 1992, MNRAS, 259, 413
Tanaka M., Kodama T., Arimoto N., Okamura S., Umetsu K., Shimasaku K., Tanaka I., Yamada T., 2005, MNRAS, 362, 268
Taylor E. N. et al., 2015, MNRAS, 446, 2144
Temi P., Brighenti F., Mathews W. G., Bregman J. D., 2004, ApJS, 151, 237
Temi P., Brighenti F., Mathews W. G., 2007, ApJ, 660, 1215
Tojeiro R., Wilkins S., Heavens A. F., Panter B., Jimenez R., 2009, ApJS, 185, 1
van den Bergh S., 1976, ApJ, 206, 883
van den Bergh S., 1988, PASP, 100, 344
Virdee J. S. et al., 2013, MNRAS, 432, 609
Vlahakis C., Dunne L., Eales S., 2005, MNRAS, 364, 1253
Wijesinghe D. B. et al., 2011, MNRAS, 410, 2291
Wijesinghe D. B. et al., 2012, MNRAS, 423, 3679
Willmer C. et al., 2006, ApJ, 647, 853
Wolf C. et al., 2009, MNRAS, 393, 1302
Wright E. L. et al., 2010, AJ, 140, 1868
Wyder T. K. et al., 2007, ApJS, 173, 293
Young L. M. et al., 2014, MNRAS, 444, 3408
Zhukovska S., 2008, PhD thesis, Heidelberg Univ.
Zhukovska S., 2014, A&A, 562, 76
Zhukovska S., Gail J.-P., Trieloff M., 2008, A&A, 479, 453

APPENDIX A: SDSS POSTAGE-STAMP IMAGES OF *RED* GALAXIES AND THEIR SED FITS

Table A1. List of all *red* galaxies detected in HATLAS.

Index	HATLAS IAU ID	SDSS OBJID	SDSS RA	SDSS Dec	NUV−r (mag)	$\log(\Sigma_5)$ (Mpc^{-2})	i (deg)	Type
1	HATLAS-J085450.2+021207	587727944563687568	$8^{h}54^{m}50^{s}.22$	$+2^{\circ}12'8''.37$	4.71	− 0.693	56.3	U
2	HATLAS-J092342.9+012056	587727942956220488	$9^{h}23^{m}42^{s}.94$	$+1^{\circ}20'57''.21$	5.06	0.099	38.67	S
3	HATLAS-J084643.5+015034	587727944025964790	$8^{h}46^{m}43^{s}.64$	$+1^{\circ}50'35''.95$	5.44	0.997	70.88	S
4	HATLAS-J084345.2−003205	588848899354329167	$8^{h}43^{m}45^{s}.22$	$-0^{\circ}32'4''.59$	5.28	− 0.08	66.09	U
5	HATLAS-J092110.3+021205	587726033304944826	$9^{h}21^{m}10^{s}.43$	$+2^{\circ}12'4''.44$	4.81	− 1.143	82.92	S
6	HATLAS-J084305.0+010858	587726032227008788	$8^{h}43^{m}5^{s}.15$	$+1^{\circ}8'55''.59$	4.66	0.055	57.29	S
7	HATLAS-J092344.2−001113	588848898895591029	$9^{h}23^{m}44^{s}.38$	$-0^{\circ}11'14''.06$	4.72	− 0.203	72.62	S
8	HATLAS-J084139.5+015346	587726033300619494	$8^{h}41^{m}39^{s}.55$	$+1^{\circ}53'46''.57$	4.7	− 0.484	34.33	U
9	HATLAS-J084343.9−001243	587725074451595552	$8^{h}43^{m}44^{s}.02$	$-0^{\circ}12'43''.98$	4.67	0.035	73.62	S
10	HATLAS-J085946.8−000019	588848899892969689	$8^{h}59^{m}46^{s}.88$	$-0^{\circ}0'20''.2$	4.75	− 0.323	69.26	S
11	HATLAS-J084713.9+012141	587727943489094075	$8^{h}47^{m}14^{s}.09$	$+1^{\circ}21'44''.65$	5.43	− 0.648	35.45	E
12	HATLAS-J090911.8+000030	587725074991218943	$9^{h}9^{m}11^{s}.88$	$+0^{\circ}0'28''.79$	5.16	− 0.644	79.06	S
13	HATLAS-J084632.0+001825	588848900428398906	$8^{h}46^{m}32^{s}.24$	$+0^{\circ}18'26''.85$	5.44	0.122	61.57	U
14	HATLAS-J090952.3−003019	588848899357147464	$9^{h}9^{m}52^{s}.4$	$-0^{\circ}30'16''.72$	4.72	− 1.013	48.67	E
15	HATLAS-J085407.6+012716	587727943489880290	$8^{h}54^{m}7^{s}.53$	$+1^{\circ}27'18''.01$	4.52	− 0.57	61.4	S
16	HATLAS-J084625.7+014913	587727944025899418	$8^{h}46^{m}25^{s}.84$	$+1^{\circ}49'11''.11$	4.92	− 0.427	53.09	U
17	HATLAS-J083610.1+005604	587727942951043325	$8^{h}36^{m}10^{s}.04$	$+0^{\circ}56'0''.54$	4.72	0.665	53.86	U
18	HATLAS-J091612.2−004200	587725073918263574	$9^{h}16^{m}12^{s}.16$	$-0^{\circ}41'58''.08$	4.8	− 0.4	56.76	S
19	HATLAS-J092158.0+023427	587727944566636774	$9^{h}21^{m}58^{s}.05$	$+2^{\circ}34'28''.44$	5.1	− 1.051	39.17	E
20	HATLAS-J084933.2+014340	587726032764600581	$8^{h}49^{m}33^{s}.08$	$+1^{\circ}43'40''.89$	4.78	− 0.227	54.61	E
21	HATLAS-J090752.4+012945	587727943491387551	$9^{h}7^{m}52^{s}.23$	$+1^{\circ}29'44''.39$	4.62	0.597	34.05	E
22	HATLAS-J090929.3+020326	587727944028455086	$9^{h}9^{m}29^{s}.56$	$+2^{\circ}3'25''.69$	5.5	− 0.356	62.22	U
23	HATLAS-J084215.5+011605	587727943488569644	$8^{h}42^{m}15^{s}.64$	$+1^{\circ}16'5''.77$	4.67	0.221	74.86	S
24	HATLAS-J084630.9+015620	587726033301143661	$8^{h}46^{m}31^{s}.0$	$+1^{\circ}56'21''.44$	4.63	− 0.706	80.33	S
25	HATLAS-J084324.4+005705	587727942951829819	$8^{h}43^{m}24^{s}.52$	$+0^{\circ}57'5''.62$	5.87	− 0.245	37.25	E
26	HATLAS-J085738.4+010741	587727942953402664	$8^{h}57^{m}38^{s}.51$	$+1^{\circ}7'41''.34$	5.02	0.702	68.5	S
27	HATLAS-J091735.1+001931	588848900431741238	$9^{h}17^{m}35^{s}.15$	$+0^{\circ}19'30''.52$	5.06	− 0.175	30.5	U
28	HATLAS-J084929.1−005350	588010931369083190	$8^{h}49^{m}29^{s}.3$	$-0^{\circ}53'44''.48$	4.58	nan	38.67	U
29	HATLAS-J085554.8−002832	588848899355639926	$8^{h}55^{m}54^{s}.59$	$-0^{\circ}28'26''.59$	6.41	0.669	46.49	E
30	HATLAS-J091333.6−001508	587725074454806843	$9^{h}13^{m}34^{s}.04$	$-0^{\circ}15'9''.56$	4.74	− 0.996	28.72	U
31	HATLAS-J091143.6+012055	587726032230154446	$9^{h}11^{m}43^{s}.76$	$+1^{\circ}20'56''.79$	4.77	− 1.367	60.52	U
32	HATLAS-J092232.9−005813	587729151452774559	$9^{h}22^{m}33^{s}.11$	$-0^{\circ}58'13''.64$	5.03	2.057	29.99	E
33	HATLAS-J085750.5−005517	587729151450022213	$8^{h}57^{m}50^{s}.7$	$-0^{\circ}55'17''.26$	4.97	0.825	68.92	S
34	HATLAS-J084043.4+010814	587726032226746692	$8^{h}40^{m}43^{s}.12$	$+1^{\circ}8'11''.83$	4.78	0.632	27.14	U
35	HATLAS-J092125.1−000341	588848898895328909	$9^{h}21^{m}25^{s}.09$	$-0^{\circ}3'43''.62$	4.86	− 0.987	61.86	S
36	HATLAS-J085311.5+005530	587727942952878410	$8^{h}53^{m}11^{s}.59$	$+0^{\circ}55'34''.59$	5.94	− 0.282	70.27	S
37	HATLAS-J085443.3+010539	587727942953074975	$8^{h}54^{m}43^{s}.22$	$+1^{\circ}5'45''.35$	5.07	− 0.578	42.14	E
38	HATLAS-J114923.8−010501	587748927628902552	$11^{h}49^{m}23^{s}.54$	$-1^{\circ}5'1''.79$	4.6	0.22	75.72	S
39	HATLAS-J115841.9−011801	587724650867523744	$11^{h}58^{m}41^{s}.95$	$-1^{\circ}18'0''.26$	4.6	− 0.833	81.55	S
40	HATLAS-J121840.2−001522	587722982815891459	$12^{h}18^{m}40^{s}.23$	$-0^{\circ}15'23''.27$	4.64	− 0.417	45.72	U
41	HATLAS-J113955.6+013042	587728307494584346	$11^{h}39^{m}55^{s}.86$	$+1^{\circ}30'43''.42$	4.62	1.267	56.1	S
42	HATLAS-J115256.8+012929	587728307495960699	$11^{h}52^{m}57^{s}.0$	$+1^{\circ}29'30''.38$	4.76	− 0.244	71.53	S
43	HATLAS-J120028.7−015138	587724650330849374	$12^{h}0^{m}28^{s}.68$	$-1^{\circ}51'38''.87$	5.21	− 0.697	47.64	E
44	HATLAS-J120844.2−003226	588848899376742632	$12^{h}8^{m}44^{s}.22$	$-0^{\circ}32'27''.03$	5.23	− 0.717	53.36	U
45	HATLAS-J120613.6−003423	588848899376480427	$12^{h}6^{m}13^{s}.54$	$-0^{\circ}34'23''.79$	4.54	− 0.44	73.63	S
46	HATLAS-J115448.1+000154	587748929240105086	$11^{h}54^{m}48^{s}.05$	$+0^{\circ}1'54''.31$	4.73	− 0.281	58.09	E
47	HATLAS-J121815.4−002151	587722982815826062	$12^{h}18^{m}15^{s}.44$	$-0^{\circ}21'53''.46$	4.63	0.002	62.11	S
48	HATLAS-J121700.2−004455	587722982278824126	$12^{h}17^{m}0^{s}.41$	$-0^{\circ}44'57''.05$	4.78	0.602	75.37	S
49	HATLAS-J115257.6+004210	588848900985651366	$11^{h}52^{m}57^{s}.73$	$+0^{\circ}42'9''.72$	5.17	− 0.396	76.79	S
50	HATLAS-J120028.9−000725	588848899912696073	$12^{h}0^{m}28^{s}.87$	$-0^{\circ}7'24''.87$	5.81	0.612	56.89	E
51	HATLAS-J115754.8+001333	588848900449304761	$11^{h}57^{m}54^{s}.83$	$+0^{\circ}13'32''.9$	4.92	0.66	71.6	S
52	HATLAS-J115442.0−005447	588848898838364283	$11^{h}54^{m}42^{s}.05$	$-0^{\circ}54'49''.15$	4.59	− 0.51	58.0	U
53	HATLAS-J114547.3−011709	587724650866081917	$11^{h}45^{m}47^{s}.33$	$-1^{\circ}17'8''.13$	4.57	0.401	65.02	S
54	HATLAS-J115525.5−002039	587748928703299628	$11^{h}55^{m}25^{s}.47$	$-0^{\circ}20'42''.63$	4.6	0.205	60.34	S
55	HATLAS-J114837.1−011246	587748927628837012	$11^{h}48^{m}37^{s}.19$	$-1^{\circ}12'46''.2$	6.28	1.702	39.33	E
56	HATLAS-J115827.6+004304	588848900986241088	$11^{h}58^{m}27^{s}.7$	$+0^{\circ}43'4''.46$	6.08	− 0.541	56.33	E
57	HATLAS-J121636.4−005723	588848898840723542	$12^{h}16^{m}36^{s}.51$	$-0^{\circ}57'21''.43$	5.19	− 0.79	63.45	E

Table A1 – *continued*

Index	HATLAS IAU ID	SDSS OBJID	SDSS RA	SDSS Dec	NUV$-r$ (mag)	$\log(\Sigma_5)$ (Mpc^{-2})	i (deg)	Type
58	HATLAS-J115122.7+000702	587748929239711890	$11^{h}51^{m}22^{s}.64$	$+0^{\circ}7'2''.43$	4.68	− 0.597	23.1	U
59	HATLAS-J121747.1+003553	587722983889502322	$12^{h}17^{m}47^{s}.17$	$+0^{\circ}35'51''.09$	4.86	− 0.583	72.32	S
60	HATLAS-J120454.4+011402	588848901523832979	$12^{h}4^{m}54^{s}.65$	$+1^{\circ}14'2''.7$	5.35	− 0.172	26.47	E
61	HATLAS-J114750.4−013710	587725041701159100	$11^{h}47^{m}50^{s}.38$	$-1^{\circ}37'11''.31$	4.86	0.558	49.64	U
62	HATLAS-J114828.1+001825	588848900448256260	$11^{h}48^{m}28^{s}.25$	$+0^{\circ}18'22''.94$	4.7	nan	56.22	E
63	HATLAS-J120212.5−014032	587724650331045959	$12^{h}2^{m}12^{s}.24$	$-1^{\circ}40'31''.17$	4.75	− 0.764	63.17	S
64	HATLAS-J114930.0−010511	587748927628902442	$11^{h}49^{m}30^{s}.15$	$-1^{\circ}5'11''.46$	5.58	0.277	39.47	E
65	HATLAS-J115053.9−010830	587722981739069591	$11^{h}50^{m}53^{s}.76$	$-1^{\circ}8'29''.65$	4.93	0.115	37.35	U
66	HATLAS-J120008.3−003950	587748928166953080	$12^{h}0^{m}8^{s}.17$	$-0^{\circ}39'48''.21$	4.94	0.066	60.54	U
67	HATLAS-J120048.1−011117	587748927630147744	$12^{h}0^{m}48^{s}.28$	$-1^{\circ}11'17''.6$	5.01	− 0.461	47.56	E
68	HATLAS-J113836.4−013713	587724650328424633	$11^{h}38^{m}36^{s}.27$	$-1^{\circ}37'14''.05$	4.52	0.554	22.58	E
69	HATLAS-J122026.8−011046	587722981742280865	$12^{h}20^{m}26^{s}.87$	$-1^{\circ}10'47''.28$	4.67	0.446	34.85	U
70	HATLAS-J120844.8+001220	587748929241612470	$12^{h}8^{m}44^{s}.83$	$+0^{\circ}12'21''.46$	4.98	− 0.572	42.44	U
71	HATLAS-J121001.7−011516	587724650868768886	$12^{h}10^{m}1^{s}.61$	$-1^{\circ}15'17''.01$	5.68	− 0.833	58.76	S
72	HATLAS-J113919.1−012012	587724650865361032	$11^{h}39^{m}18^{s}.95$	$-1^{\circ}20'18''.19$	5.05	− 0.521	55.2	U
73	HATLAS-J114318.5−004414	587748928165118125	$11^{h}43^{m}18^{s}.61$	$-0^{\circ}44'17''.11$	4.53	− 0.539	51.33	U
74	HATLAS-J120140.5+005138	587748930314567848	$12^{h}1^{m}40^{s}.15$	$+0^{\circ}51'38''.71$	5.01	− 0.644	61.67	U
75	HATLAS-J121823.6−013038	587725041704501421	$12^{h}18^{m}23^{s}.51$	$-1^{\circ}30'37''.86$	4.83	− 0.167	59.44	U
76	HATLAS-J120535.5+010445	588848901523898501	$12^{h}5^{m}35^{s}.33$	$+1^{\circ}4'44''.34$	5.53	0.479	49.35	U
77	HATLAS-J114526.8−002708	588848899374186712	$11^{h}45^{m}26^{s}.58$	$-0^{\circ}27'11''.56$	5.32	− 0.914	29.57	E
78	HATLAS-J114849.6−005941	588848898837708980	$11^{h}48^{m}49^{s}.57$	$-0^{\circ}59'40''.53$	4.88	− 0.6	53.97	U
79	HATLAS-J114609.3−010205	588848898837446812	$11^{h}46^{m}9^{s}.18$	$-1^{\circ}2'6''.83$	4.88	0.585	63.8	S
80	HATLAS-J120246.1+002207	588848900449829017	$12^{h}2^{m}46^{s}.51$	$+0^{\circ}22'3''.61$	6.64	− 0.207	53.62	S
81	HATLAS-J120406.6+001411	588848900449960274	$12^{h}4^{m}6^{s}.52$	$+0^{\circ}14'9''.77$	4.98	− 0.117	72.22	S
82	HATLAS-J145112.4−002724	588848899394568318	$14^{h}51^{m}12^{s}.4$	$-0^{\circ}27'24''.76$	4.71	0.187	75.01	S
83	HATLAS-J143224.5+005041	587722984441118986	$14^{h}32^{m}24^{s}.62$	$+0^{\circ}50'41''.14$	4.9	− 0.133	86.81	S
84	HATLAS-J141501.6−005136	588848898853699826	$14^{h}15^{m}1^{s}.74$	$-0^{\circ}51'36''.46$	5.33	− 0.412	82.77	S
85	HATLAS-J143143.3−011418	587729972324073647	$14^{h}31^{m}43^{s}.38$	$-1^{\circ}14'19''.78$	4.84	− 1.137	77.59	S
86	HATLAS-J143801.4−001217	588848899929997456	$14^{h}38^{m}1^{s}.53$	$-0^{\circ}12'18''.13$	4.65	− 0.479	69.75	S
87	HATLAS-J141126.2+011711	587726014009573415	$14^{h}11^{m}26^{s}.23$	$+1^{\circ}17'11''.47$	5.55	0.777	19.37	E
88	HATLAS-J142004.5−001852	587722982829130030	$14^{h}20^{m}4^{s}.67$	$-0^{\circ}18'53''.29$	4.6	0.053	33.78	U
89	HATLAS-J141611.6+015204	587726032263446738	$14^{h}16^{m}11^{s}.83$	$+1^{\circ}52'4''.72$	5.5	− 0.575	62.73	U
90	HATLAS-J143012.5+001400	588848900465951018	$14^{h}30^{m}12^{s}.5$	$+0^{\circ}14'2''.81$	4.81	0.855	58.65	S
91	HATLAS-J144810.4+012203	587726014550442257	$14^{h}48^{m}10^{s}.5$	$+1^{\circ}22'1''.93$	4.57	− 0.393	68.64	S
92	HATLAS-J141446.6−000417	588848899927441586	$14^{h}14^{m}46^{s}.6$	$-0^{\circ}4'17''.37$	5.26	− 0.764	59.98	S
93	HATLAS-J142926.0+012315	587726031728017631	$14^{h}29^{m}26^{s}.06$	$+1^{\circ}23'16''.62$	4.56	− 0.658	57.74	S
94	HATLAS-J141727.9+002857	587722983902609591	$14^{h}17^{m}27^{s}.97$	$+0^{\circ}28'57''.99$	5.19	0.713	40.76	E
95	HATLAS-J141310.5+014618	587726014546641064	$14^{h}13^{m}10^{s}.5$	$+1^{\circ}46'17''.11$	5.57	2.006	44.1	E
96	HATLAS-J144224.0+005430	587722984442232848	$14^{h}42^{m}23^{s}.61$	$+0^{\circ}54'28''.79$	5.01	− 0.433	41.32	E
97	HATLAS-J142113.4−002756	588848899391226106	$14^{h}21^{m}13^{s}.45$	$-0^{\circ}27'59''.63$	4.94	− 0.479	32.78	E
98	HATLAS-J142015.8+010252	587722984439808094	$14^{h}20^{m}15^{s}.91$	$+1^{\circ}2'51''.5$	4.81	0.17	65.57	S
99	HATLAS-J141539.0−002649	588848899390636315	$14^{h}15^{m}39^{s}.07$	$-0^{\circ}26'51''.7$	4.85	− 0.098	57.74	U
100	HATLAS-J142429.3+015829	587726015084757174	$14^{h}24^{m}29^{s}.34$	$+1^{\circ}58'31''.01$	4.82	0.175	74.27	S
101	HATLAS-J142856.4+002130	588848900465819923	$14^{h}28^{m}56^{s}.56$	$+0^{\circ}21'32''.39$	5.67	− 0.635	25.6	E
102	HATLAS-J142613.8−011122	587729972323483911	$14^{h}26^{m}13^{s}.74$	$-1^{\circ}11'24''.01$	5.29	0.195	39.73	E
103	HATLAS-J143052.0+011836	587726031728214195	$14^{h}30^{m}52^{s}.04$	$+1^{\circ}18'34''.61$	4.97	− 0.672	71.24	S
104	HATLAS-J143731.7+000341	587722983367901556	$14^{h}37^{m}31^{s}.92$	$+0^{\circ}3'39''.01$	4.63	− 0.87	72.71	S
105	HATLAS-J144532.2−010921	587729972325646543	$14^{h}45^{m}32^{s}.17$	$-1^{\circ}9'20''.9$	4.75	− 0.757	79.16	S
106	HATLAS-J144346.1+004306	588848901004329189	$14^{h}43^{m}46^{s}.24$	$+0^{\circ}43'4''.43$	4.59	− 0.767	61.13	U
107	HATLAS-J140753.5−001931	587722982827819184	$14^{h}7^{m}53^{s}.34$	$-0^{\circ}19'27''.74$	4.5	− 0.396	27.39	E
108	HATLAS-J142831.0+014541	587726032264822925	$14^{h}28^{m}31^{s}.19$	$+1^{\circ}45'40''.78$	5.53	− 0.599	35.48	E
109	HATLAS-J144718.4−010621	587729972325843159	$14^{h}47^{m}18^{s}.4$	$-1^{\circ}6'18''.83$	4.63	0.055	48.6	E
110	HATLAS-J142517.4−010304	587722981755977936	$14^{h}25^{m}17^{s}.4$	$-1^{\circ}3'6''.24$	5.18	0.139	33.86	U
111	HATLAS-J142437.5−013819	587729971786481829	$14^{h}24^{m}37^{s}.35$	$-1^{\circ}38'20''.15$	5.4	0.688	31.13	E
112	HATLAS-J145123.6+000025	587722983369474066	$14^{h}51^{m}23^{s}.42$	$+0^{\circ}0'25''.48$	4.94	− 0.627	44.69	E
113	HATLAS-J141353.0−004527	587722982291603595	$14^{h}13^{m}53^{s}.48$	$-0^{\circ}45'27''.18$	5.07	0.484	22.97	E
114	HATLAS-J141325.9−004923	587722982291538161	$14^{h}13^{m}25^{s}.85$	$-0^{\circ}49'23''.89$	5.12	0.36	43.99	E
115	HATLAS-J145216.9+010631	587726014014030018	$14^{h}52^{m}16^{s}.66$	$+1^{\circ}6'34''.3$	5.01	− 0.721	32.7	E
116	HATLAS-J142512.3−001858	587722982829719819	$14^{h}25^{m}12^{s}.49$	$-0^{\circ}19'0''.67$	4.92	− 0.287	47.84	E
117	HATLAS-J141516.7−003941	587722982291734808	$14^{h}15^{m}16^{s}.49$	$-0^{\circ}39'40''.61$	5.29	− 0.088	70.96	S

Table A2. MAGPHYS output parameters for the *red* galaxies having *WISE* observed photometric data.

Index	HATLAS IAU ID	$\log(M_*/M_\odot)$	$\log(\mathrm{SFR})$ ($M_\odot\,\mathrm{yr}^{-1}$)	$\log(\mathrm{SFR}/M_*)$ (yr^{-1})	$\log(M_D/M_\odot)$	$\log(M_D/M_*)$	f_μ
1	HATLAS-J114923.8−010501	10.92	− 0.09	− 11.01	7.51	− 3.41	0.72
2	HATLAS-J115841.9−011801	10.98	0.32	− 10.66	8.08	− 2.89	0.78
3	HATLAS-J121840.2−001522	11.29	− 0.21	− 11.5	7.77	− 3.52	0.78
4	HATLAS-J113955.6+013042	11.2	− 0.04	− 11.25	7.82	− 3.38	0.67
5	HATLAS-J115256.8+012929	10.61	− 0.25	− 10.86	7.97	− 2.64	0.78
6	HATLAS-J120028.7−015138	10.95	− 0.79	− 11.75	7.87	− 3.08	0.83
7	HATLAS-J120844.2−003226	11.05	− 1.04	− 12.08	7.39	− 3.65	0.82
8	HATLAS-J120613.6−003423	10.59	0.02	− 10.57	7.35	− 3.24	0.68
9	HATLAS-J115448.1+000154	11.02	− 0.35	− 11.37	8.11	− 2.9	0.78
10	HATLAS-J121815.4−002151	10.51	− 2.67	− 13.18	7.32	− 3.18	0.98
11	HATLAS-J121700.2−004455	10.68	− 0.84	− 11.52	7.86	− 2.83	0.74
12	HATLAS-J115257.6+004210	10.85	− 0.62	− 11.47	7.82	− 3.03	0.8
13	HATLAS-J120028.9−000725	11.35	− 0.87	− 12.22	7.86	− 3.49	0.8
14	HATLAS-J115754.8+001333	10.55	− 0.34	− 10.89	7.44	− 3.11	0.86
15	HATLAS-J115442.0−005447	10.66	− 2.27	− 12.93	8.28	− 2.37	0.85
16	HATLAS-J114547.3−011709	10.68	− 0.23	− 10.91	8.05	− 2.63	0.72
17	HATLAS-J115525.5−002039	11.11	0.2	− 10.91	7.67	− 3.44	0.74
18	HATLAS-J114837.1−011246	11.52	− 1.37	− 12.89	8.26	− 3.27	0.86
19	HATLAS-J115827.6+004304	10.92	− 2.85	− 13.77	6.65	− 4.26	0.85
20	HATLAS-J121636.4−005723	10.9	− 1.41	− 12.31	7.1	− 3.8	0.84
21	HATLAS-J115122.7+000702	10.88	− 0.63	− 11.51	6.87	− 4.01	0.64
22	HATLAS-J121747.1+003553	10.71	− 0.46	− 11.17	7.3	− 3.41	0.76
23	HATLAS-J120454.4+011402	11.02	− 1.03	− 12.05	7.41	− 3.61	0.8
24	HATLAS-J114750.4−013710	10.71	− 0.95	− 11.66	7.16	− 3.55	0.94
25	HATLAS-J114828.1+001825	11.14	− 0.16	− 11.3	7.78	− 3.36	0.99
26	HATLAS-J120212.5−014032	10.95	− 0.54	− 11.49	8.07	− 2.88	0.83
27	HATLAS-J114930.0−010511	10.81	− 1.89	− 12.69	6.46	− 4.35	0.82
28	HATLAS-J115053.9−010830	10.73	− 0.64	− 11.37	8.2	− 2.53	0.75
29	HATLAS-J120008.3−003950	9.6	− 1.77	− 11.36	5.91	− 3.69	0.16
30	HATLAS-J120048.1−011117	10.83	− 0.44	− 11.27	8.06	− 2.77	0.69
31	HATLAS-J113836.4−013713	10.89	− 0.59	− 11.48	6.87	− 4.02	0.68
32	HATLAS-J122026.8−011046	10.68	− 1.45	− 12.13	7.56	− 3.13	0.85
33	HATLAS-J121001.7−011516	10.29	− 2.43	− 12.72	7.32	− 2.97	0.85
34	HATLAS-J113919.1−012012	10.5	− 1.19	− 11.69	7.36	− 3.15	0.84
35	HATLAS-J114318.5−004414	10.54	− 0.69	− 11.23	7.21	− 3.34	0.71
36	HATLAS-J120140.5+005138	10.94	− 0.65	− 11.58	7.41	− 3.53	0.91
37	HATLAS-J121823.6−013038	10.57	− 1.14	− 11.72	6.95	− 3.63	0.84
38	HATLAS-J120535.5+010445	10.75	− 1.54	− 12.29	7.36	− 3.39	0.99
39	HATLAS-J114526.8−002708	10.99	− 1.13	− 12.11	7.2	− 3.78	0.86
40	HATLAS-J114849.6−005941	11.25	− 0.43	− 11.68	7.54	− 3.71	1.0
41	HATLAS-J114609.3−010205	10.66	− 0.89	− 11.55	7.57	− 3.1	0.87
42	HATLAS-J120246.1+002207	11.27	− 1.42	− 12.69	7.66	− 3.61	0.81
43	HATLAS-J120406.6+001411	10.92	− 0.61	− 11.53	6.93	− 3.99	0.81
44	HATLAS-J145112.4−002724	10.63	− 0.44	− 11.07	7.68	− 2.95	0.75
45	HATLAS-J143224.5+005041	11.29	0.03	− 11.26	8.38	− 2.91	0.79
46	HATLAS-J141501.6−005136	10.61	− 0.79	− 11.4	7.37	− 3.24	0.81
47	HATLAS-J143143.3−011418	10.6	− 0.43	− 11.02	6.98	− 3.61	0.73
48	HATLAS-J143801.4−001217	10.95	0.02	− 10.93	8.11	− 2.84	0.79
49	HATLAS-J141126.2+011711	11.03	− 1.51	− 12.54	6.87	− 4.16	0.88
50	HATLAS-J142004.5−001852	10.36	− 0.21	− 10.57	7.05	− 3.31	0.71
51	HATLAS-J141611.6+015204	11.03	− 1.88	− 12.91	8.12	− 2.91	0.85
52	HATLAS-J143012.5+001400	10.69	− 0.69	− 11.38	7.37	− 3.32	0.76
53	HATLAS-J144810.4+012203	9.89	− 0.96	− 10.85	6.56	− 3.33	0.72
54	HATLAS-J142926.0+012315	11.09	− 0.17	− 11.27	7.88	− 3.21	0.71
55	HATLAS-J141727.9+002857	10.97	− 1.35	− 12.31	7.15	− 3.81	0.96
56	HATLAS-J141310.5+014618	11.03	− 0.83	− 11.86	6.96	− 4.06	0.72
57	HATLAS-J144224.0+005430	10.95	− 0.84	− 11.79	6.85	− 4.1	0.82
58	HATLAS-J142113.4−002756	11.09	− 0.29	− 11.38	7.53	− 3.56	0.83
59	HATLAS-J142015.8+010252	10.9	− 0.06	− 10.96	7.52	− 3.38	0.77
60	HATLAS-J141539.0−002649	10.73	− 0.44	− 11.17	7.32	− 3.41	0.78

Table A2 – *continued*

Index	HATLAS IAU ID	log $(M_*/\mathrm{M}_{\odot})$	log (SFR) [$\mathrm{M}_{\odot}\,\mathrm{yr}^{-1}$]	log (SFR/M_*) [yr^{-1}]	log $(M_\mathrm{D}/\mathrm{M}_{\odot})$	log (M_D/M_*)	f_μ
61	HATLAS-J142429.3+015829	10.19	− 0.75	− 10.94	6.78	− 3.4	0.76
62	HATLAS-J142856.4+002130	11.45	− 0.39	− 11.83	7.88	− 3.57	0.78
63	HATLAS-J142613.8−011122	10.87	− 0.78	− 11.65	6.93	− 3.95	0.8
64	HATLAS-J143052.0+011836	11.19	− 0.05	− 11.24	8.01	− 3.18	0.74
65	HATLAS-J143731.7+000341	10.59	− 0.43	− 11.02	7.19	− 3.4	0.73
66	HATLAS-J144532.2−010921	10.38	− 1.19	− 11.57	7.32	− 3.05	0.96
67	HATLAS-J144346.1+004306	10.25	− 0.65	− 10.89	6.77	− 3.47	0.64
68	HATLAS-J140753.5−001931	10.91	− 0.64	− 11.55	6.92	− 3.98	0.75
69	HATLAS-J142831.0+014541	11.06	− 1.06	− 12.11	7.5	− 3.56	0.88
70	HATLAS-J144718.4−010621	11.2	− 0.08	− 11.28	7.51	− 3.68	0.88
71	HATLAS-J142517.4−010304	11.06	− 0.55	− 11.61	7.65	− 3.41	0.84
72	HATLAS-J142437.5−013819	11.0	− 0.86	− 11.86	7.28	− 3.72	0.76
73	HATLAS-J145123.6+000025	10.1	− 1.39	− 11.49	6.04	− 4.06	0.69
74	HATLAS-J141353.0−004527	11.17	− 0.64	− 11.81	7.86	− 3.31	0.85
75	HATLAS-J141325.9−004923	10.87	− 0.73	− 11.6	7.94	− 2.93	0.78
76	HATLAS-J145216.9+010631	11.06	− 0.4	− 11.46	7.2	− 3.86	0.77
77	HATLAS-J142512.3−001858	10.95	− 1.16	− 12.11	7.65	− 3.3	0.86
78	HATLAS-J141516.7−003941	10.93	− 1.44	− 12.37	7.65	− 3.28	1.0

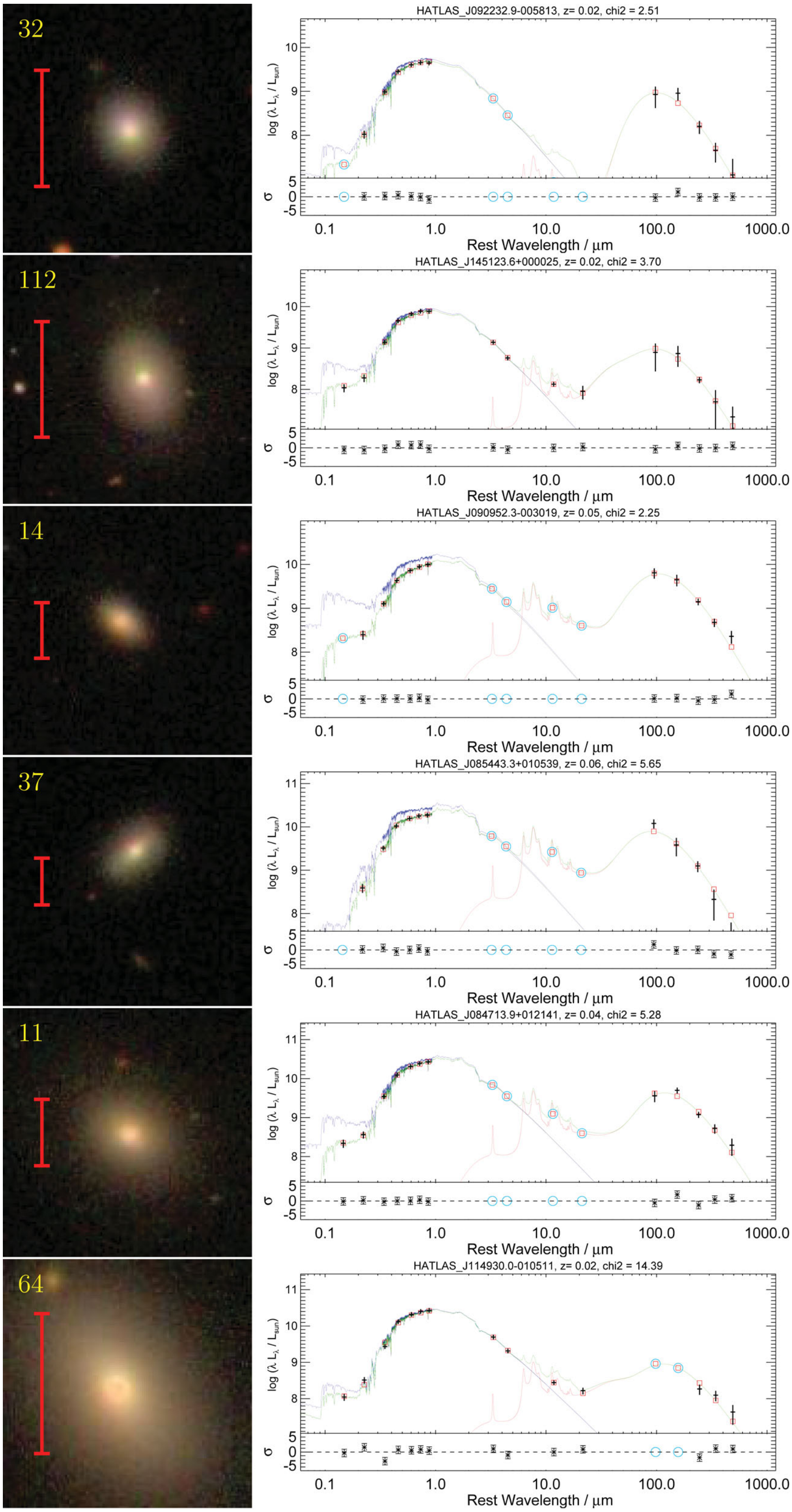

Figure A1. Gallery of optically red galaxies detected in H-ATLAS. The galaxies are sorted according to their optical morphological classification (elliptical, disc-like/edge-on and uncertain). The colour of the 10 kpc scale bar corresponds to the classification: elliptical–red, disc-like – blue and uncertain are green. Within each group the galaxies are sorted according to increasing stellar mass. We show for each galaxy the optical image (left) from SDSS (http://cas.sdss.org/dr7/en/tools/chart/list.asp) and the full UV to submm SED including the best-fitting MAGPHYS SED (right). The identification number in the top left corresponds to the row-number in Table A1.

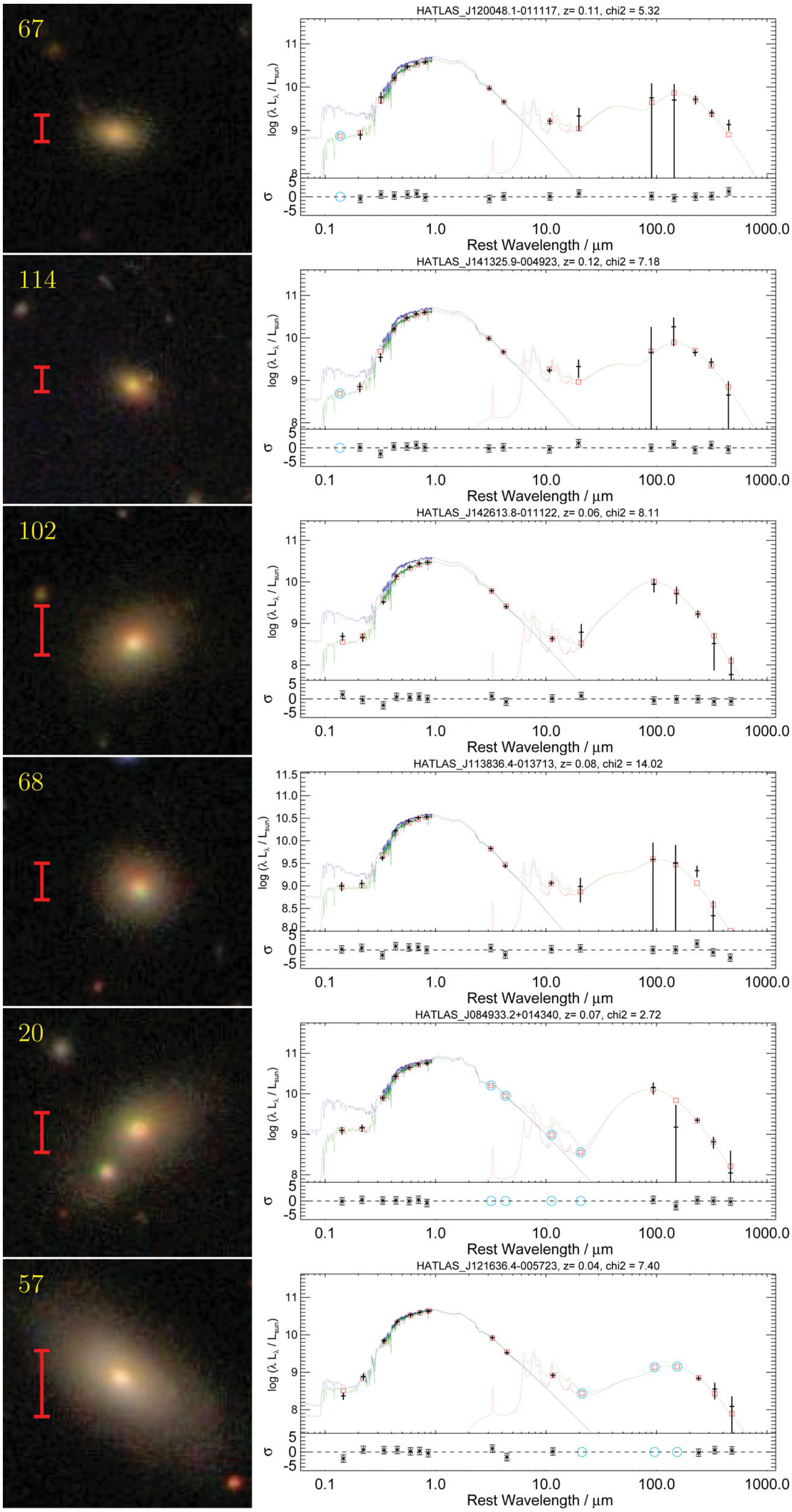

Figure A1 – *continued*

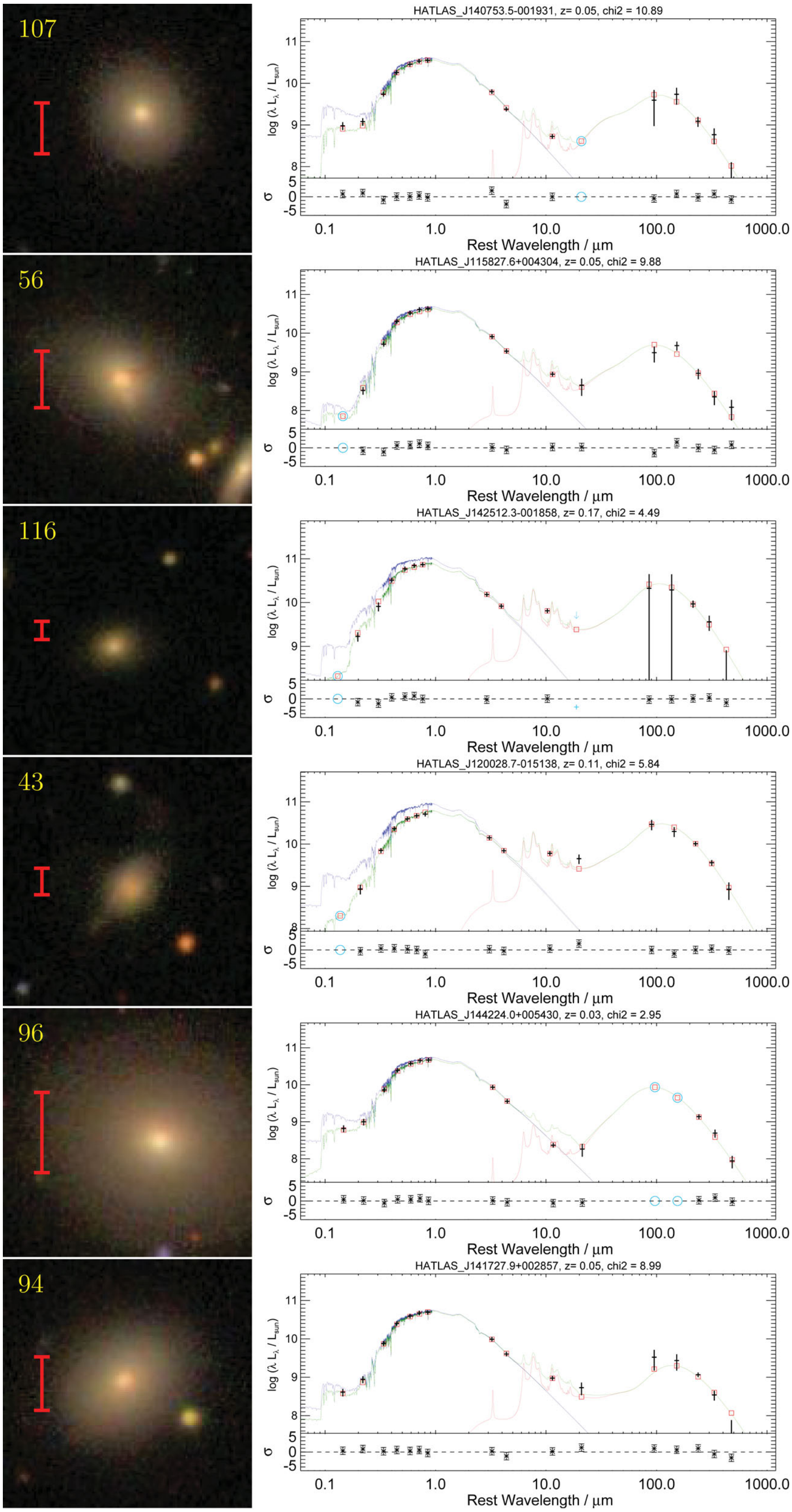

Figure A1 – *continued*

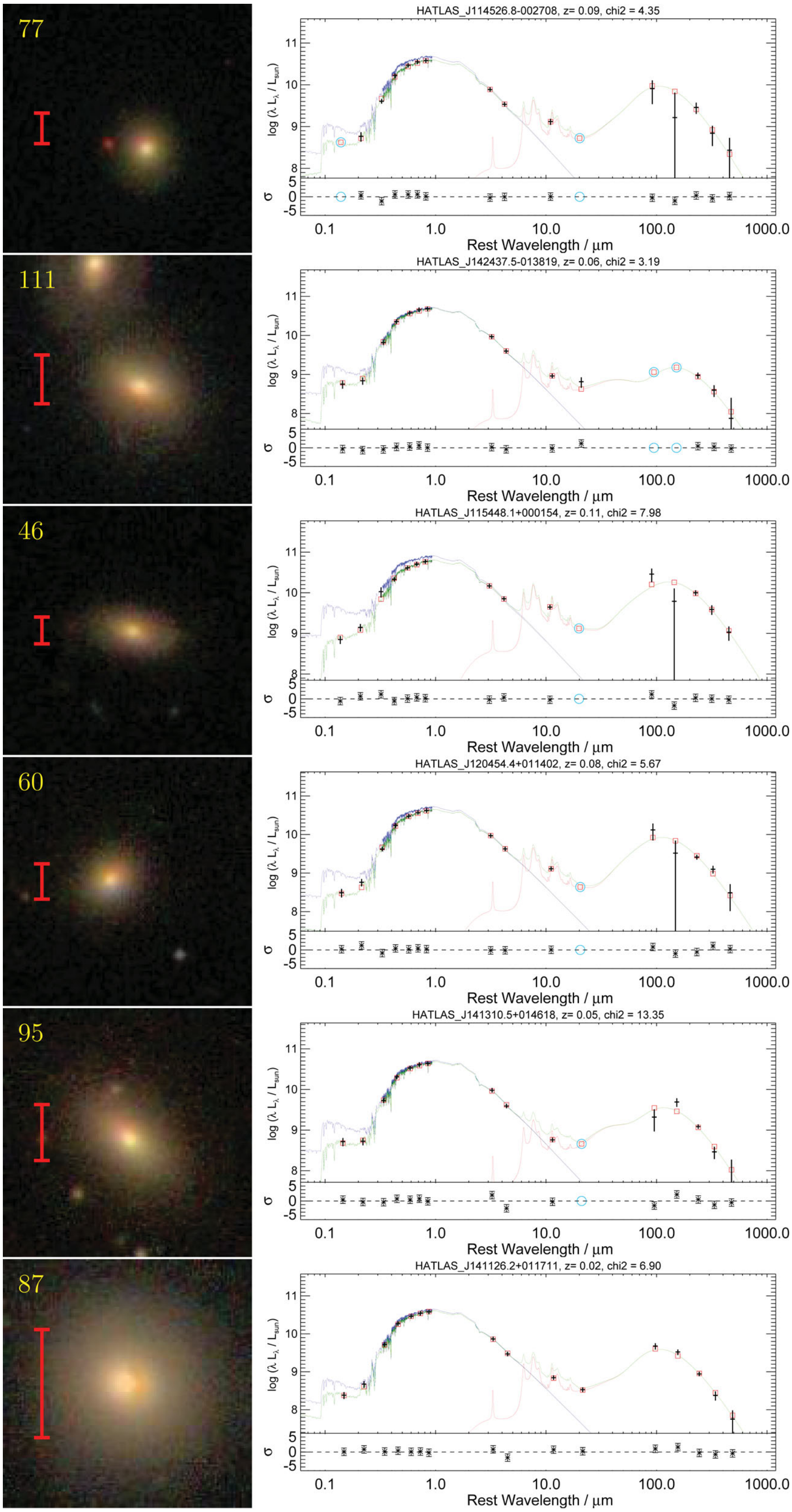

Figure A1 – *continued*

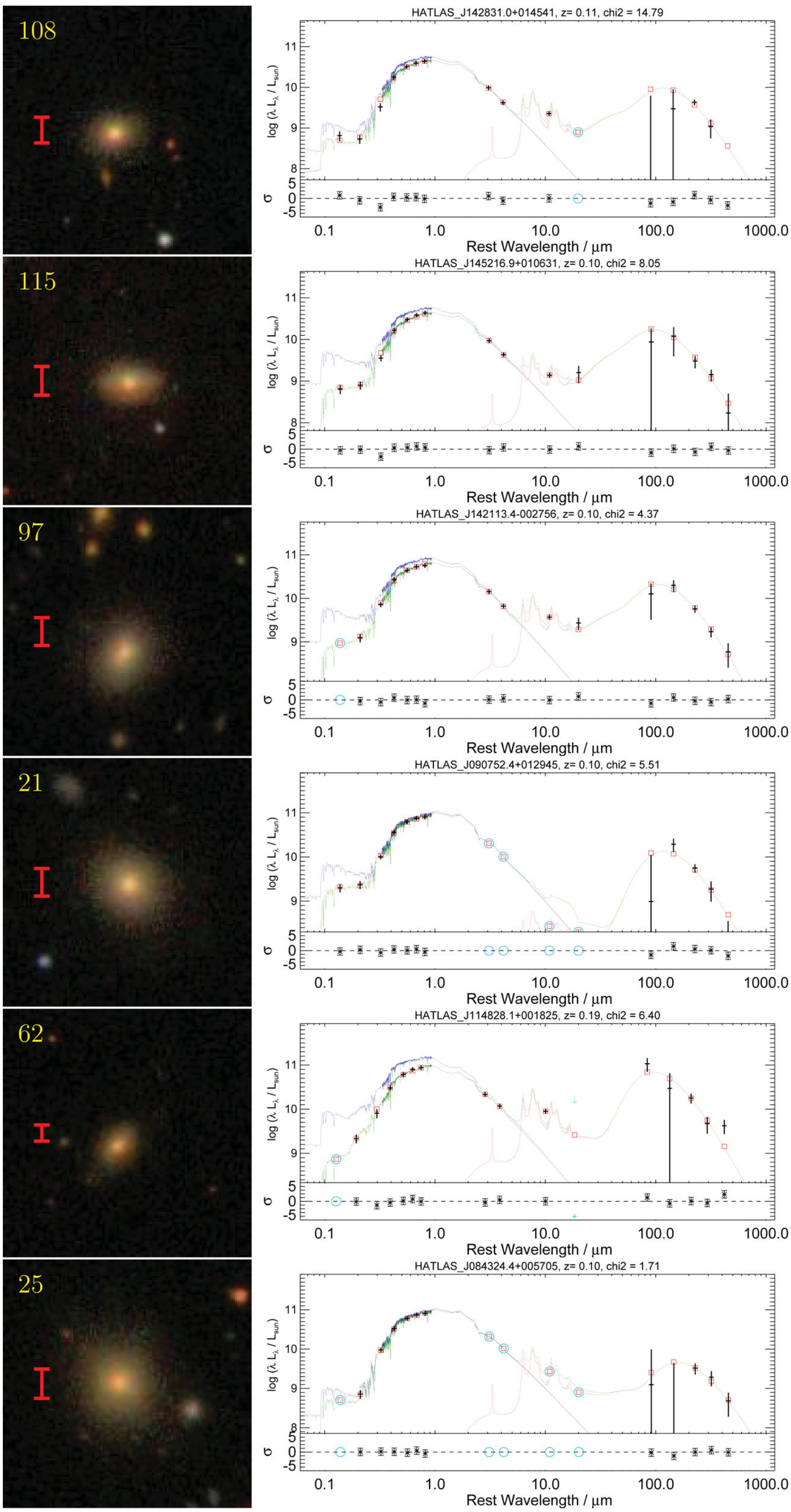

Figure A1 – *continued*

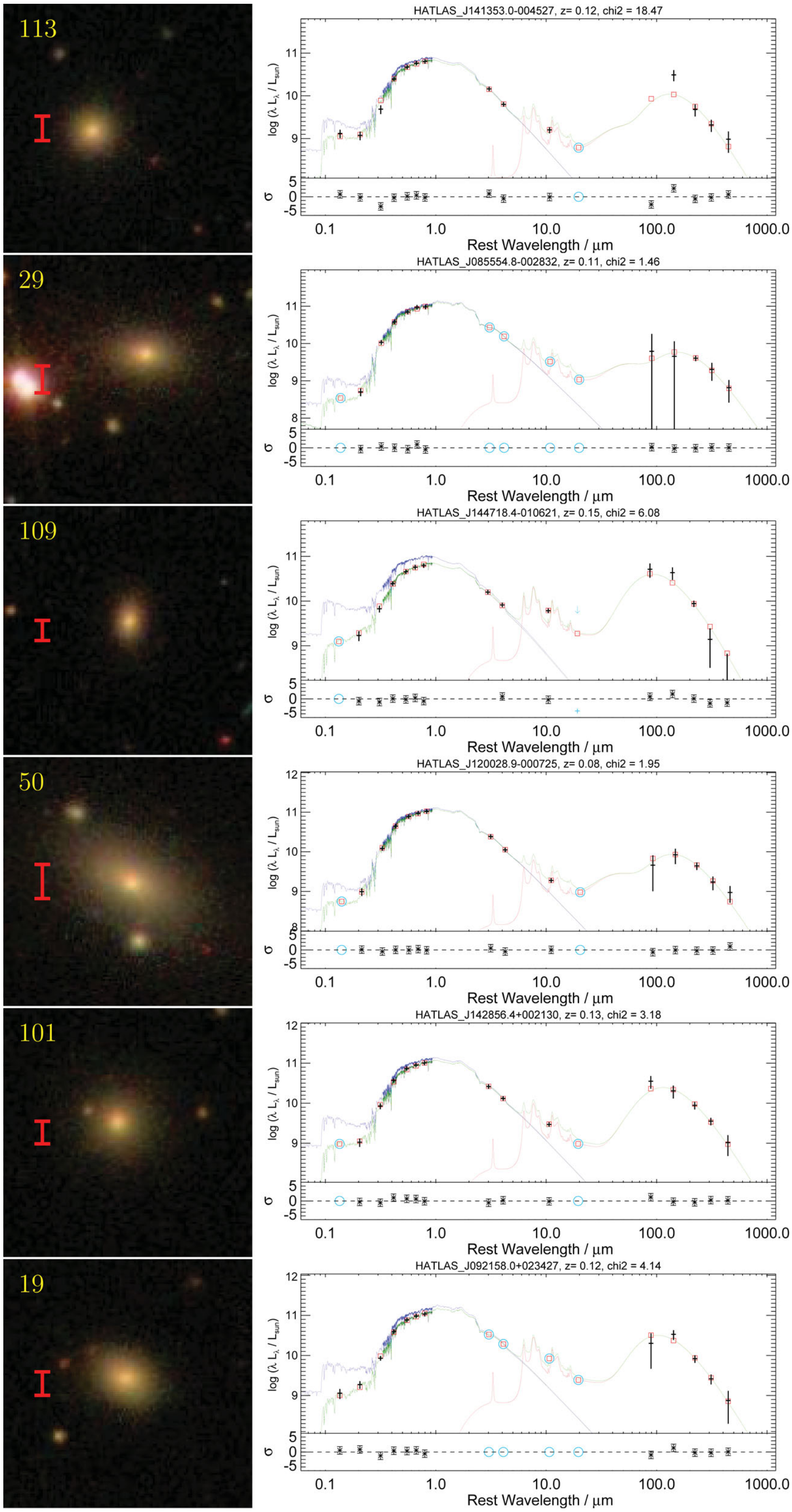

Figure A1 – *continued*

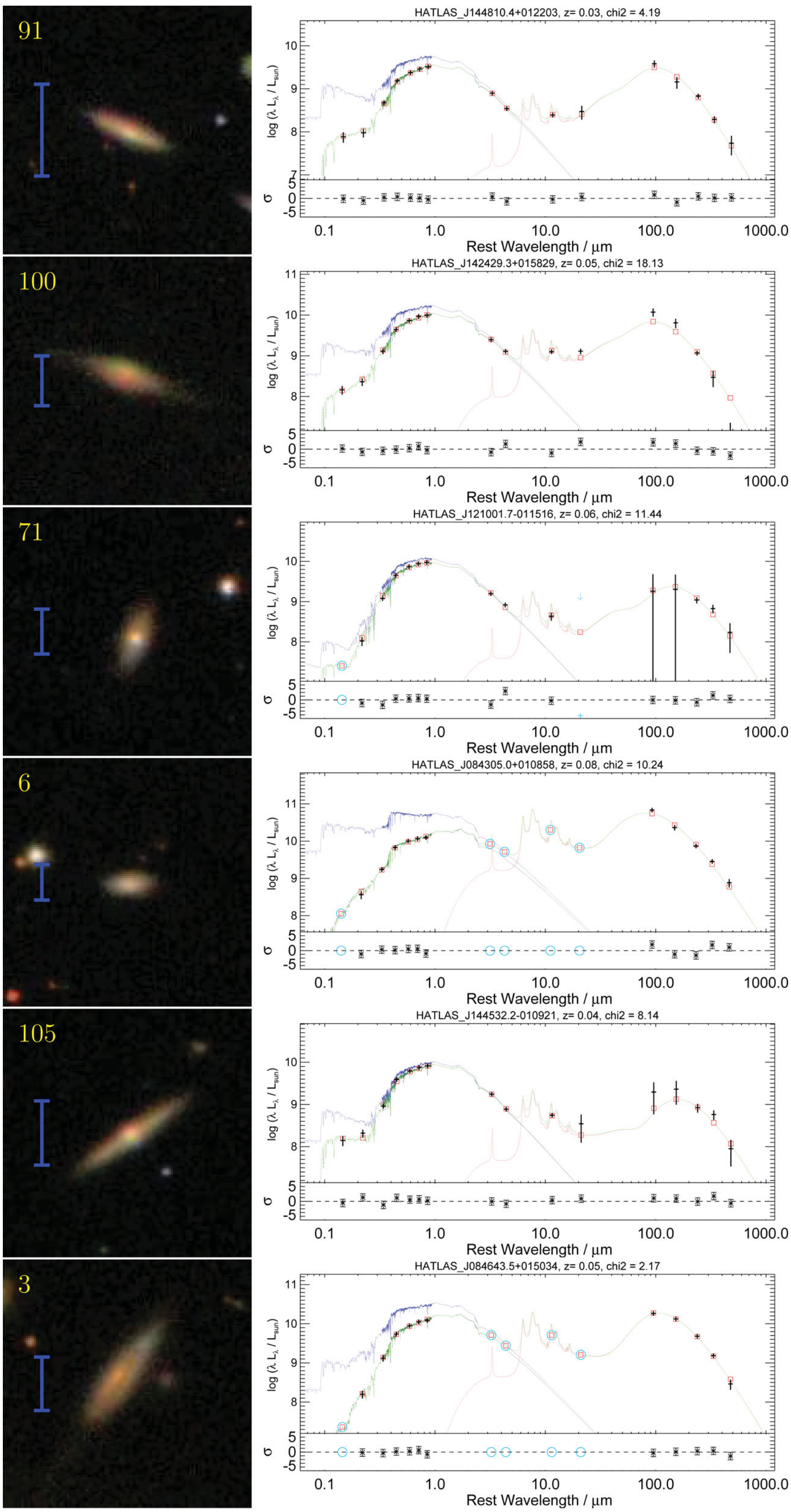

Figure A1 – *continued*

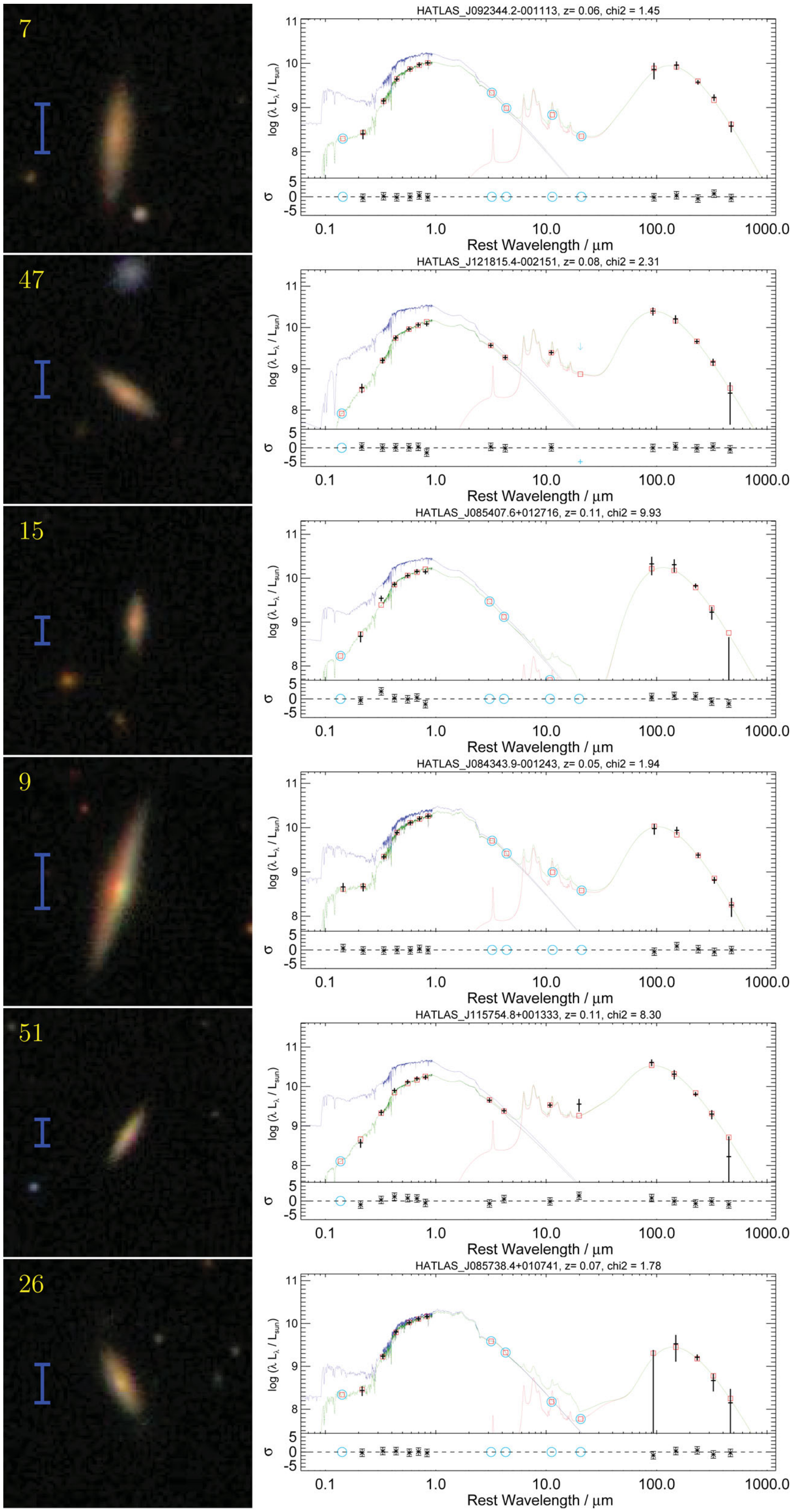

Figure A1 – *continued*

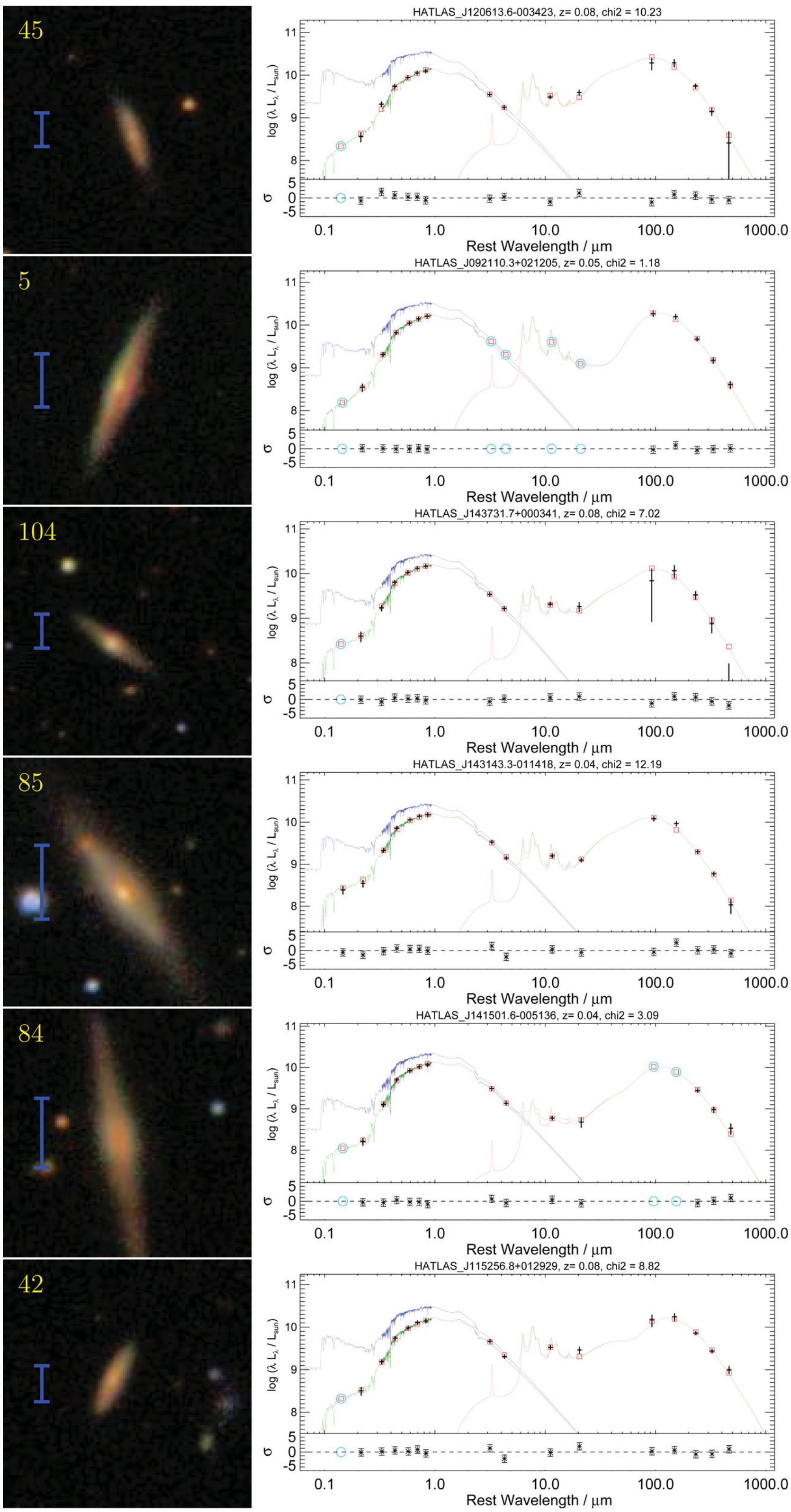

Figure A1 – *continued*

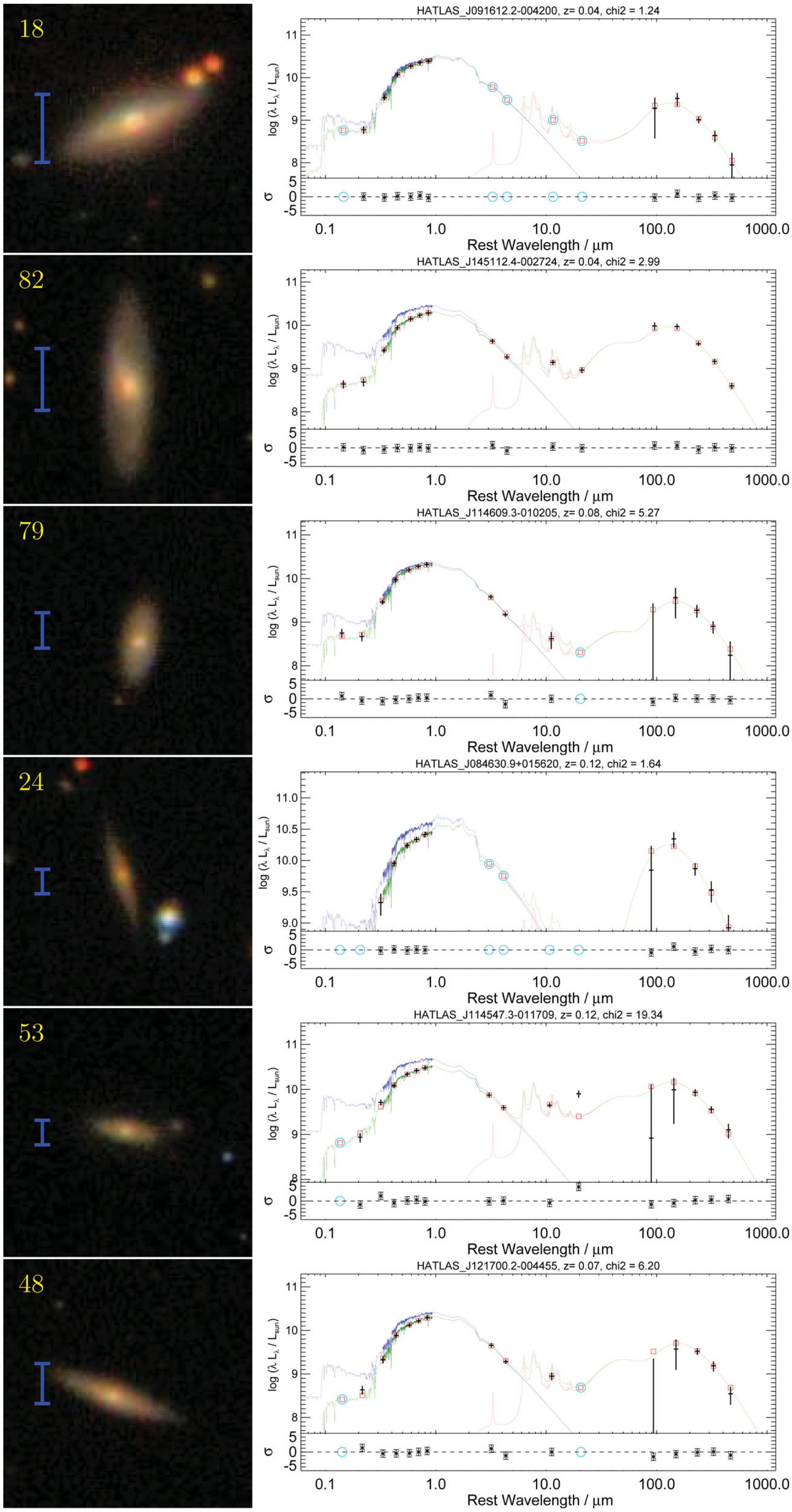

Figure A1 – *continued*

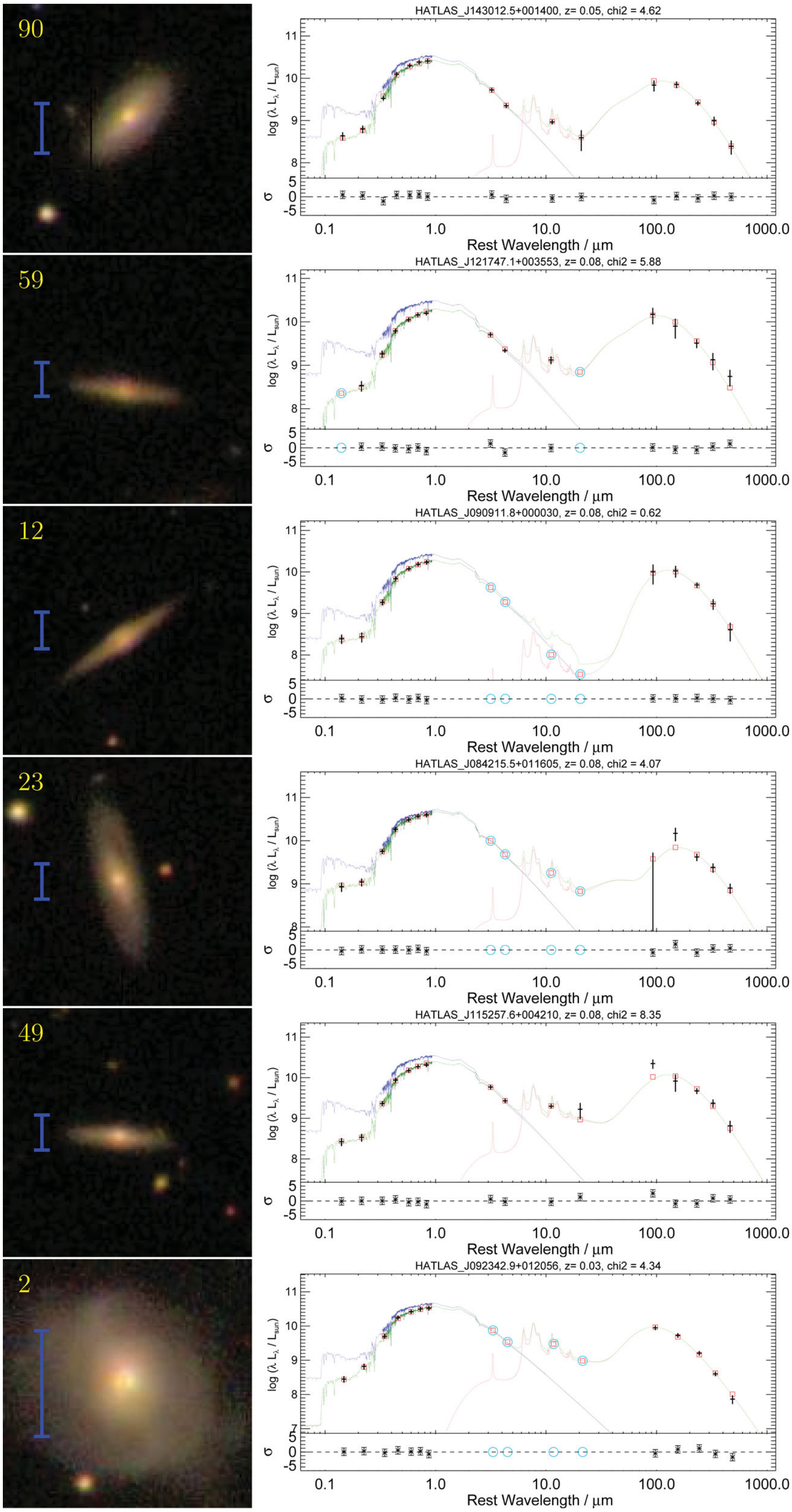

Figure A1 – *continued*

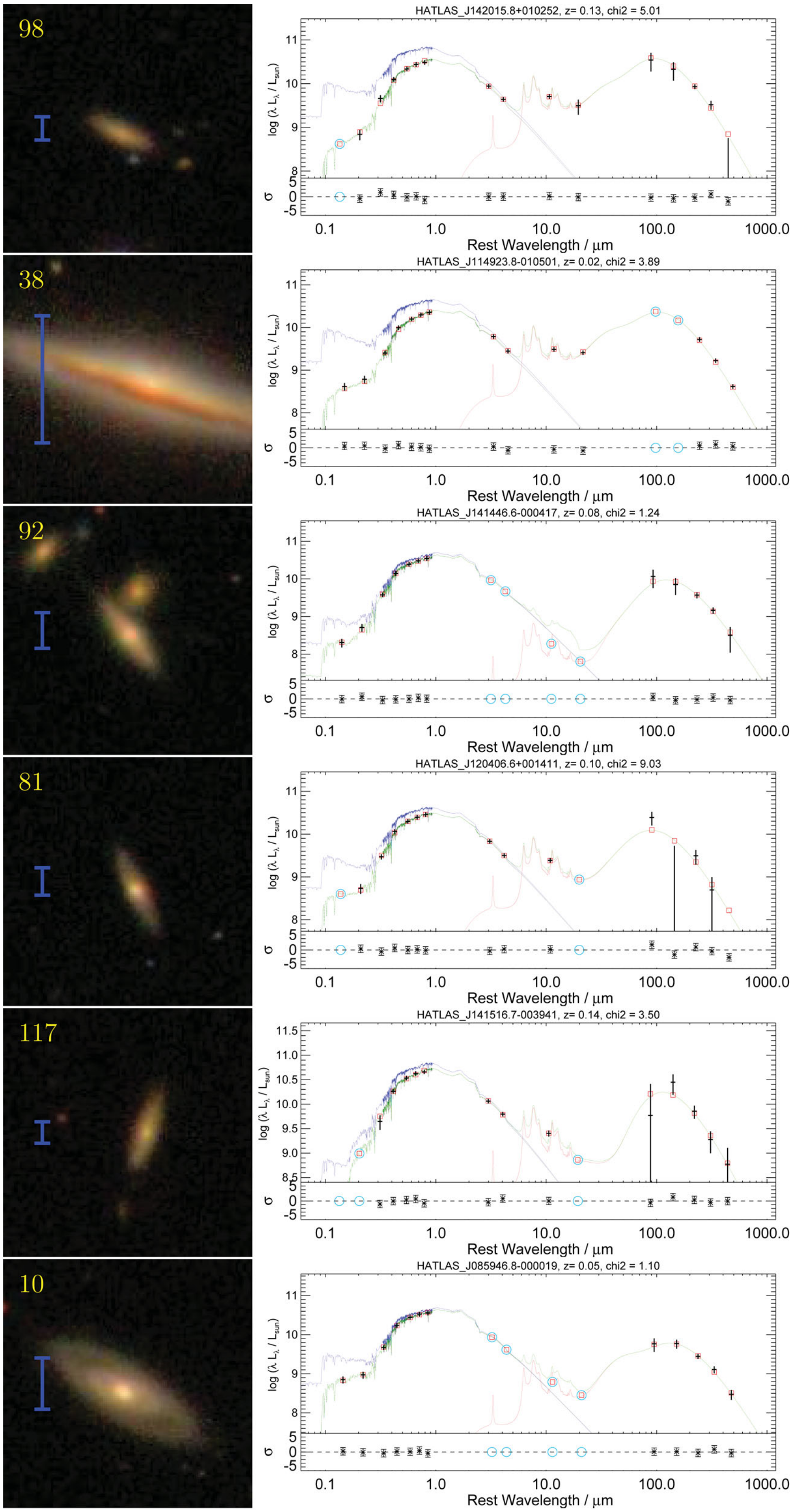

Figure A1 – *continued*

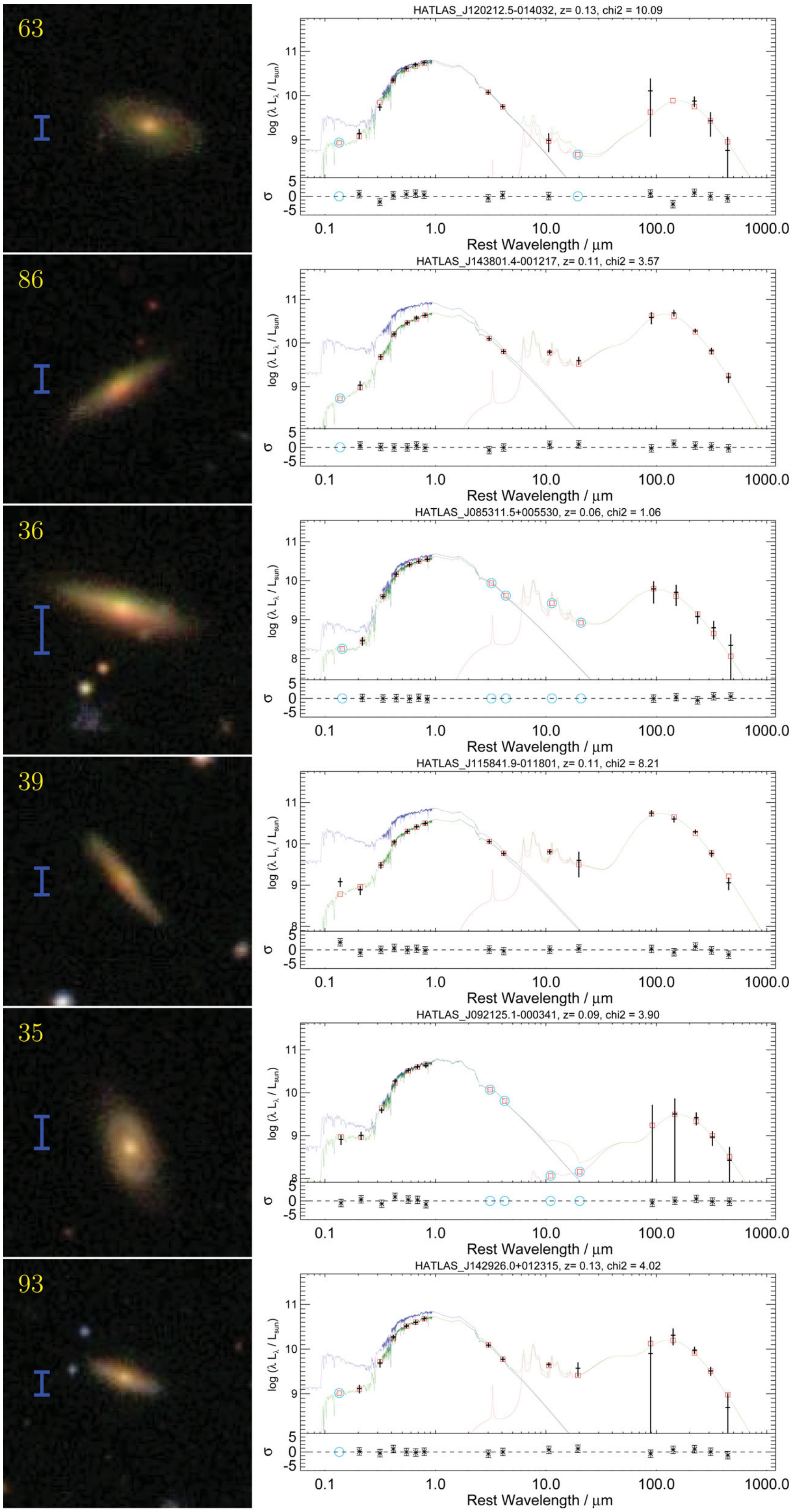

Figure A1 – *continued*

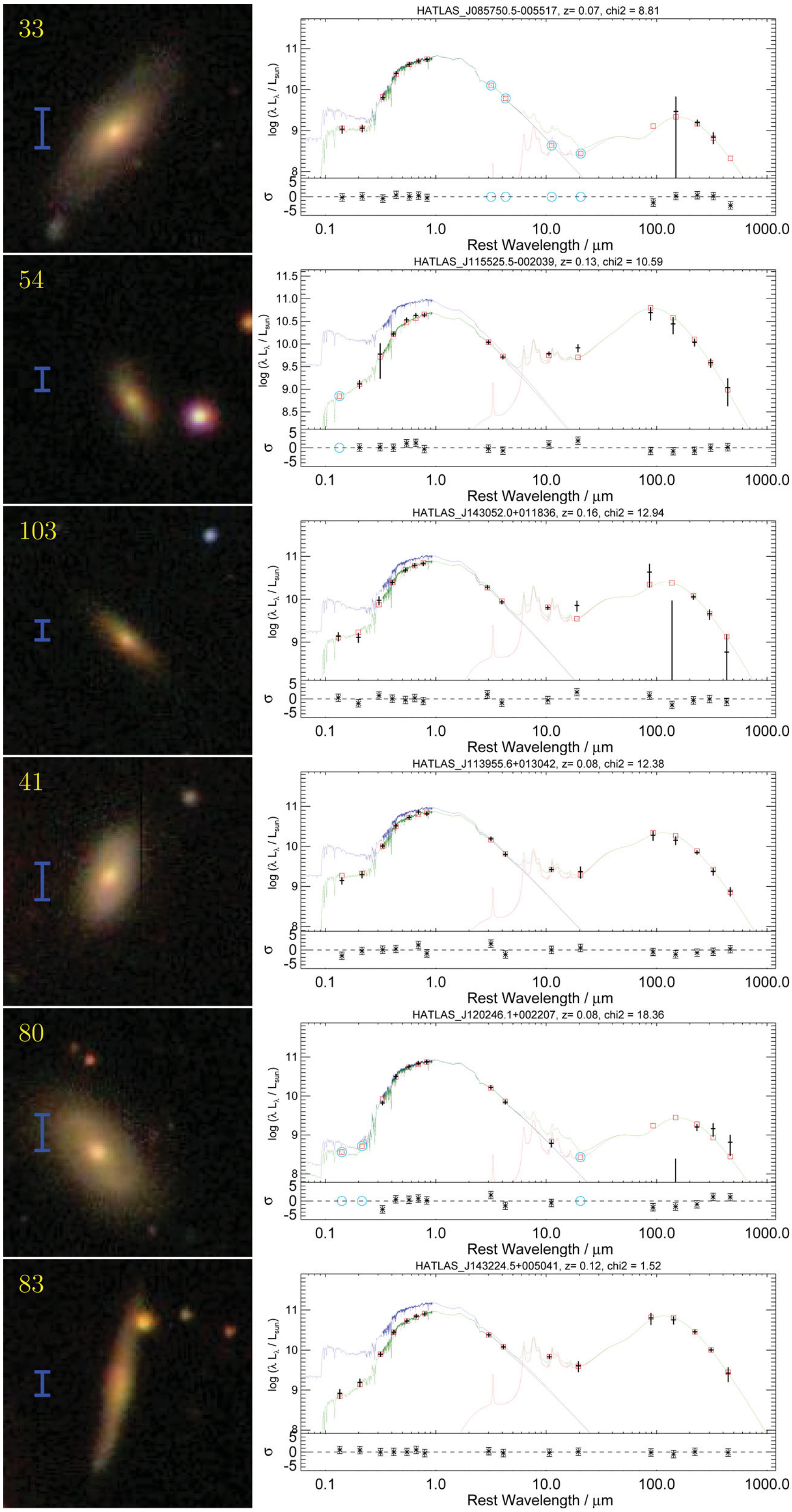

Figure A1 – *continued*

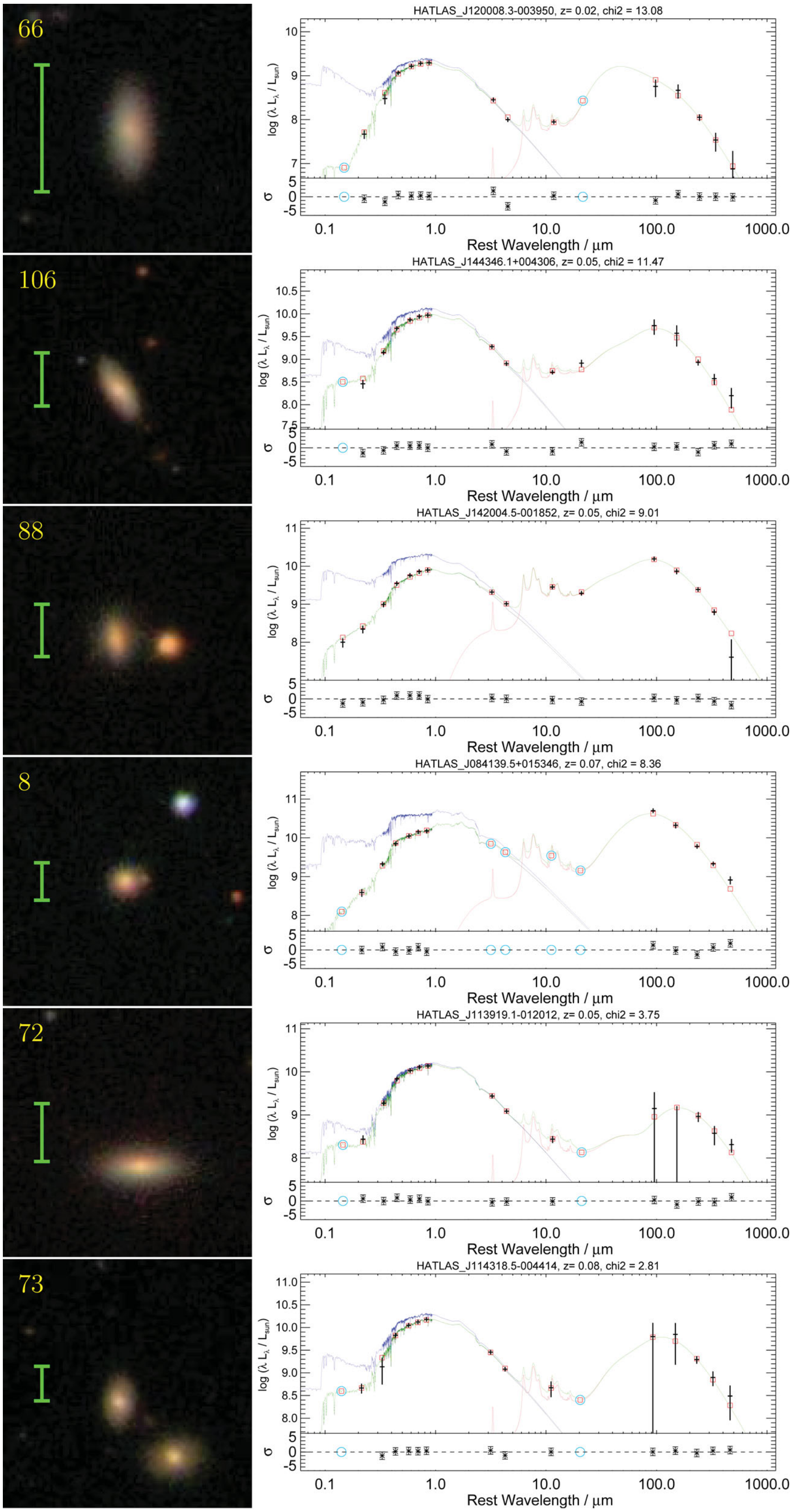

Figure A1 – *continued*

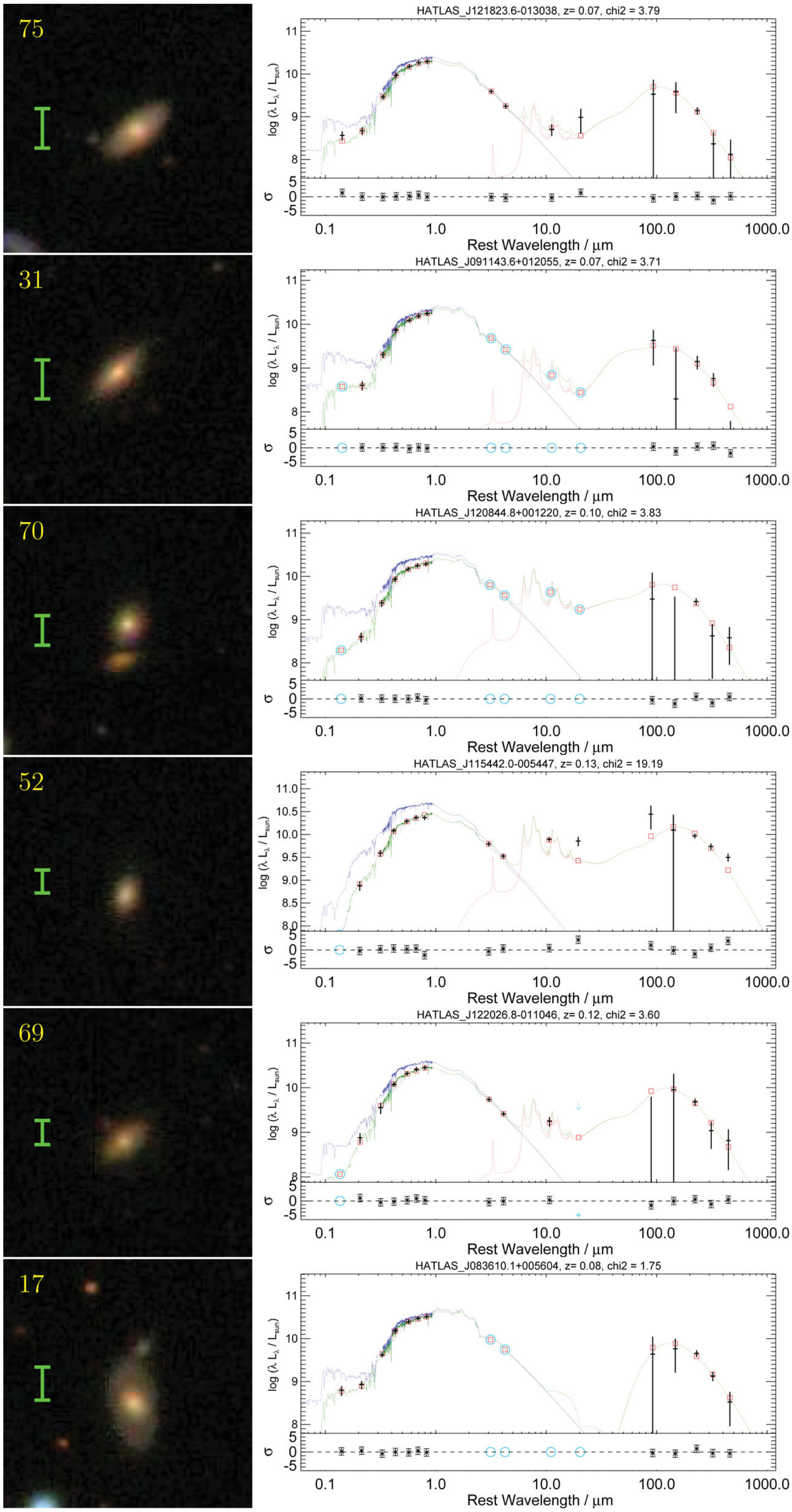

Figure A1 – *continued*

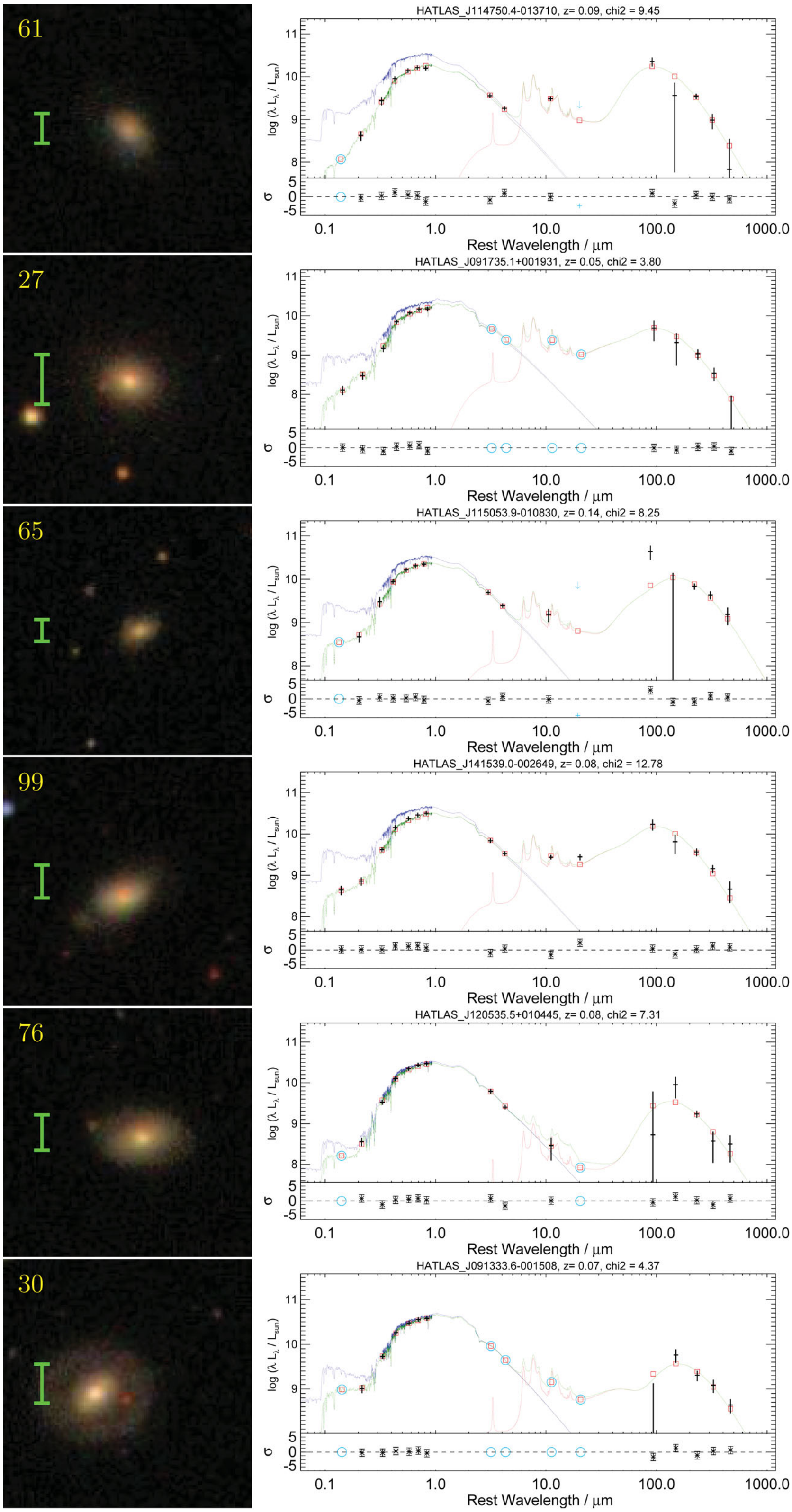

Figure A1 – *continued*

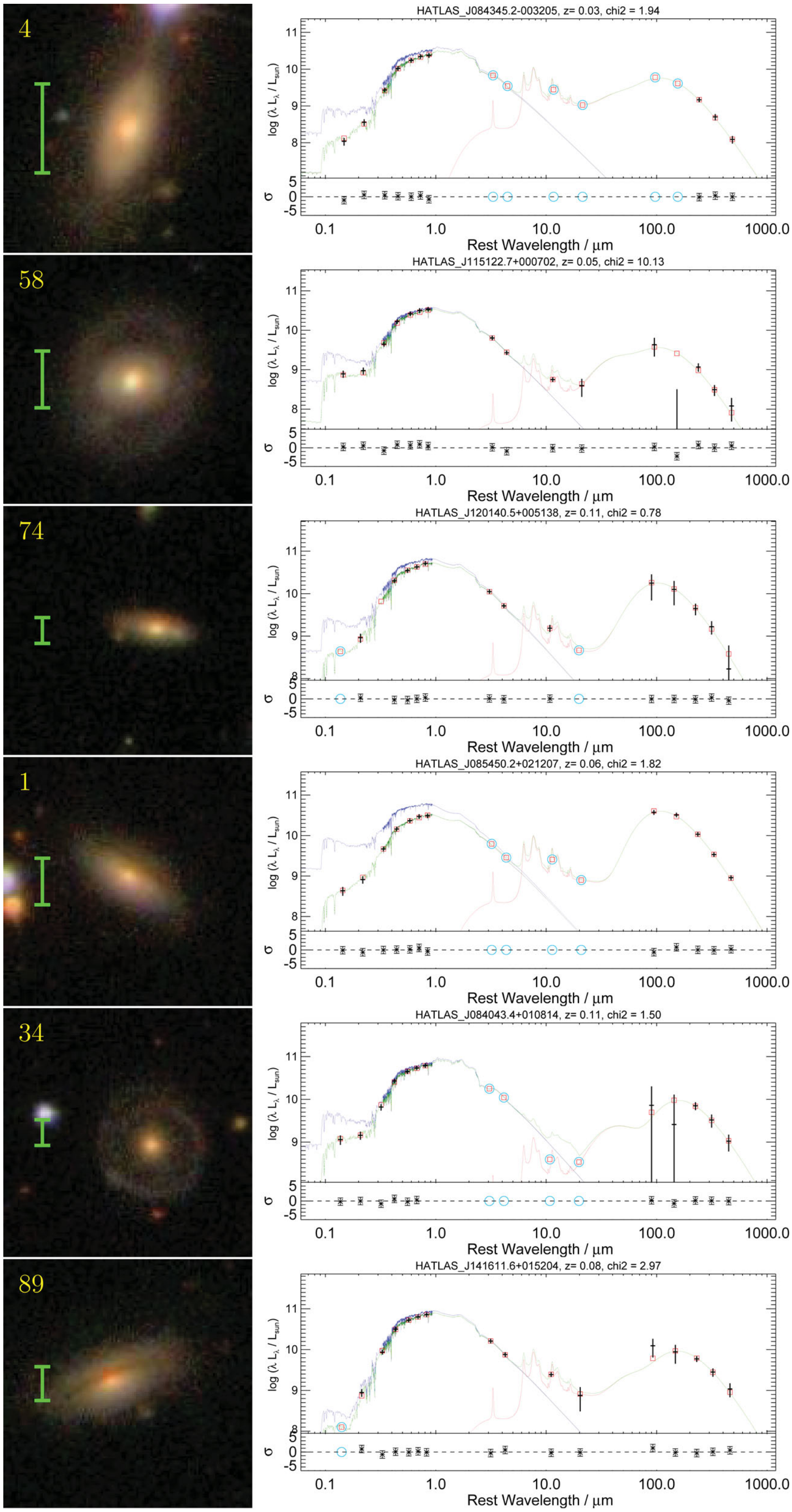

Figure A1 – *continued*

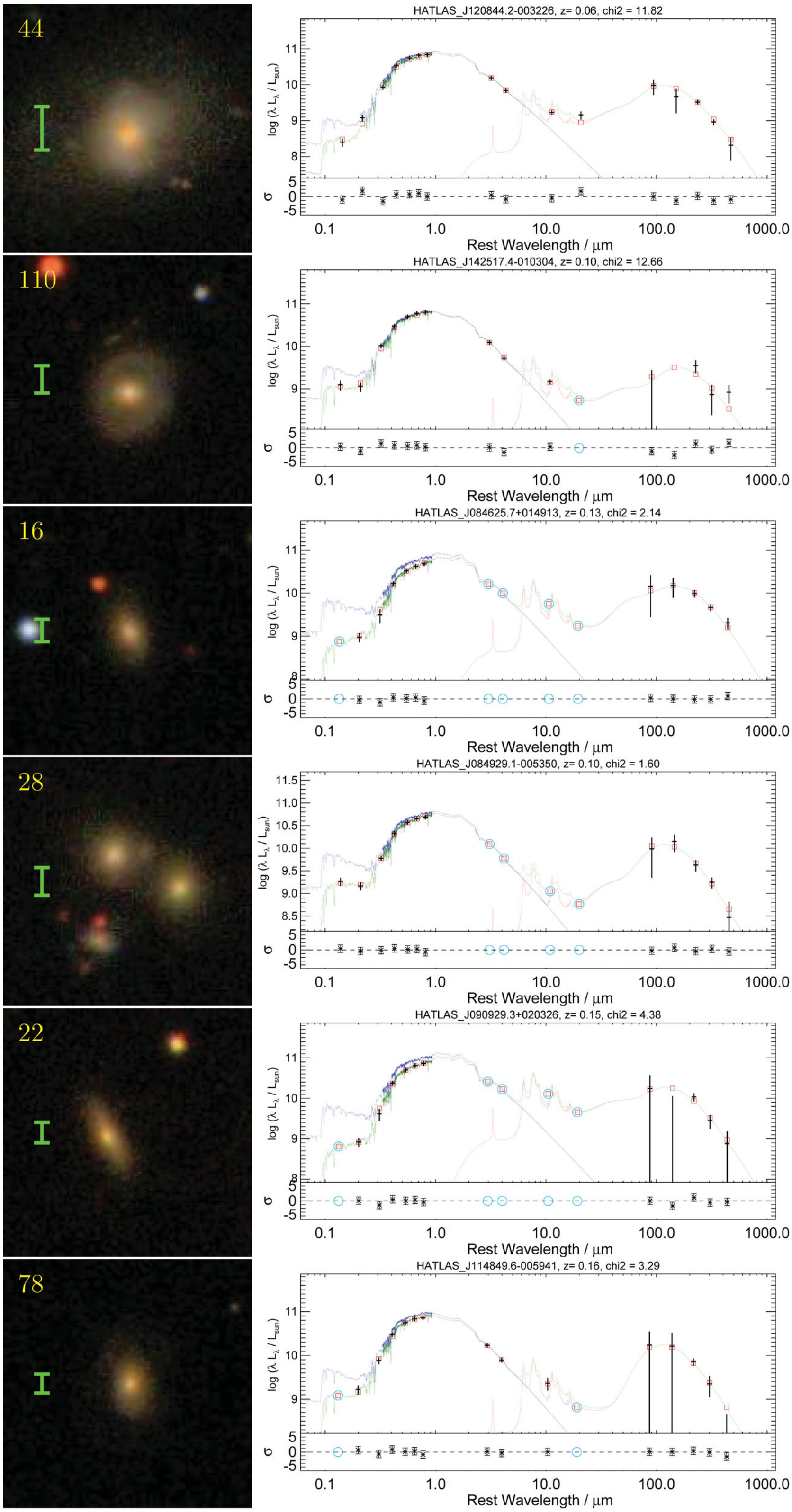

Figure A1 – *continued*

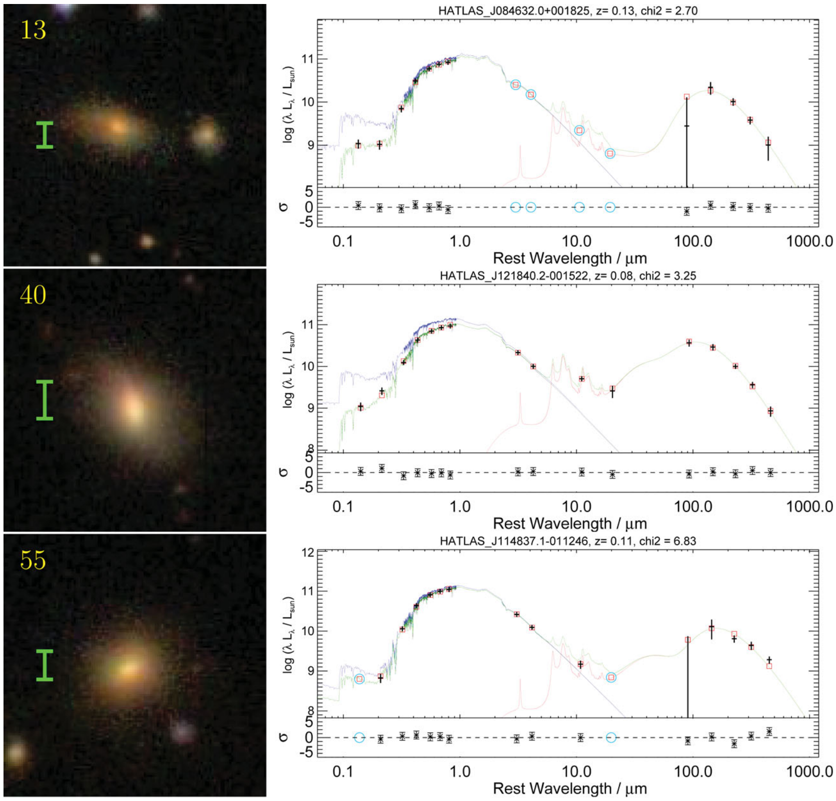

Figure A1 – *continued*

[1]*Institute of Astronomy, University of Cambridge, Madingley Road, Cambridge CB3 0HA, UK*
[2]*Niels Bohr Institute & Centre for Star and Planet Formation, University of Copenhagen, Øster Voldgade 5-7., DK-1350 Copenhagen, Denmark*
[3]*Zentrum für Astronomie der Universität Heidelberg, Institut für Theoretische Astrophysik, Albert-Ueberle-Straße 2, D-69120 Heidelberg, Germany*
[4]*Centre for Astrophysics, Science & Technology Research Institute, University of Hertfordshire, Hatfield, Herts AL10 9AB, UK*
[5]*Max-Planck-Institut für Astrophysik, Karl-Schwarzschild-Str. 1, D-85741 Garching, Germany*
[6]*Department of Physics and Astronomy, University of Canterbury, Private Bag 4800, Christchurch 8140, NZ*
[7]*Institute for Astronomy, University of Edinburgh, Royal Observatory, Blackford Hill, Edinburgh EH9 3HJ, UK*
[8]*School of Physics and Astronomy, Cardiff University, the Parade, Cardiff CF24 3AA, UK*
[9]*Max Planck Institut fuer Kernphysik, Saupfercheckweg 1, D-69117 Heidelberg, Germany*
[10]*Sterrenkundig Observatorium, Universiteit Gent, Krijgslaan 281S9, B-9000 Gent, Belgium*
[11]*Astrophysics Research Institute, Liverpool John Moores University, IC2, Liverpool Science Park, 146 Brownlow Hill, Liverpool L3 5RF, UK*
[12]*Australian Astronomical Observatory, PO Box 915, North Ryde, NSW 1670, Australia*
[13]*Sydney Institute for Astronomy, School of Physics A28, University of Sydney, NSW 2006, Australia*
[14]*Australian Astronomical Observatory, PO Box 296, Epping, NSW 1710, Australia*
[15]*Observatoire de Genève, Université de Genève, 51 Ch. des Maillettes, CH-1290 Versoix, Switzerland*
[16]*Physics Department, Imperial College London, Prince Consort Road, London SW7 2AZ, UK*
[17]*University of the Western Cape, Robert Sobukwe Road, Bellville 7535, South Africa*
[18]*Department of Physics and Astronomy, University of California, Irvine, CA 92697, USA*
[19]*INAF-Osservatorio Astronomico di Padova, Vicolo Osservatorio 5, I-35122 Padova, Italy, and SISSA, Via Bonomea 265, I-34136 Trieste, Italy*
[20]*International Centre for Radio Astronomy Research (ICRAR),University of Western Australia, 35 Stirling Highway, Crawley,WA 6009, Australia*
[21]*School of Physics & Astronomy, University of St Andrews, North Haugh, St Andrews, Fife KY16 9SS, UK*
[22]*Department of Physical Sciences, The Open University, Milton Keynes MK7 6AA, UK*
[23]*Oxford Astrophysics, Denys Wilkinson Building, University of Oxford, Keble Rd, Oxford OX1 3RH, UK*
[24]*Institut für Astro- und Teilchenphysik, Universität Innsbruck, Technikerstraße 25, A-6020 Innsbruck, Austria*
[25]*Instituto de Astronomía, Universidad Nacional Autnoma de México, A.P. 70-264, 04510 México, D.F., México*
[26]*European Southern Observatory, Karl-Schwarzschild-Str. 2, D-85748 Garching, Germany*
[27]*Department of Physics and Astronomy, University of Sussex, Brighton BN1 9RH, UK*
[28]*Observatories of the Carnegie Institution for Science, 813 Santa Barbara Street, Pasadena, CA 91101, USA*
[29]*SUPA, Institute for Astronomy, University of Edinburgh, Royal Observatory, Edinburgh EH9 3HJ, UK*
[30]*RAL Space, STFC Rutherford Appleton Laboratory, Harwell Oxford, Didcot, Oxon OX11 0QX, UK*
[31]*Jeremiah Horrocks Institute, University of Central Lancashire, Preston PR1 2HE, UK*
[32]*The Astronomical Institute of the Romanian Academy, Str. Cutitul de Argint 5, Bucharest 040557, Romania*
[33]*Finnish Centre for Astronomy with ESO (FINCA), University of Turku, Väisäläntie 20, FI-21500 Piikkiö, Finland*
[34]*School of Physics, the University of Melbourne, Parkville, VIC 3010, Australia*

This paper has been typeset from a TEX/LATEX file prepared by the author.